星系团中AGN的反馈

徐海光

物理与天文学院

hgxu@sjtu.edu.cn   hgxu.physics.sjtu.edu.cn

上海交通大学
SHANGHAI JIAO TONG UNIVERSITY

1、星系团和星系群

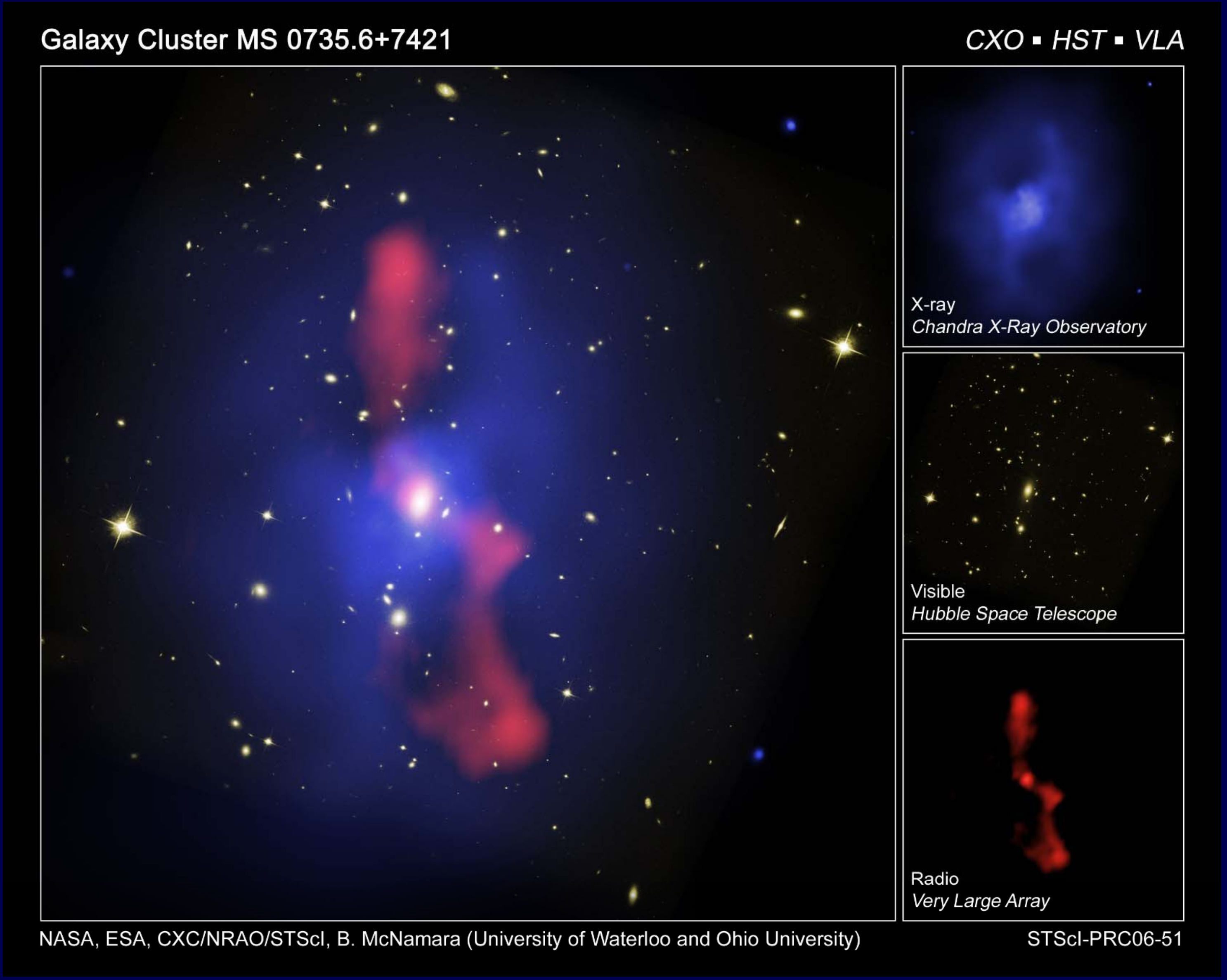

Galaxy Cluster MS 0735.6+7421
CXO ▪ HST ▪ VLA
X-ray
Chandra X-Ray Observatory
Visible
Hubble Space Telescope
Radio
Very Large Array
NASA, ESA, CXC/NRAO/STScI, B. McNamara (University of Waterloo and Ohio University)
STScI-PRC06-51

1.1、星系团的结构 ICM物理特性

- 星系团 → 星系群 → 椭圆星系
- 热动力学 + 热力学 + 化学
  → 结构&演化、星系、宇宙学
- 图像 + 光谱

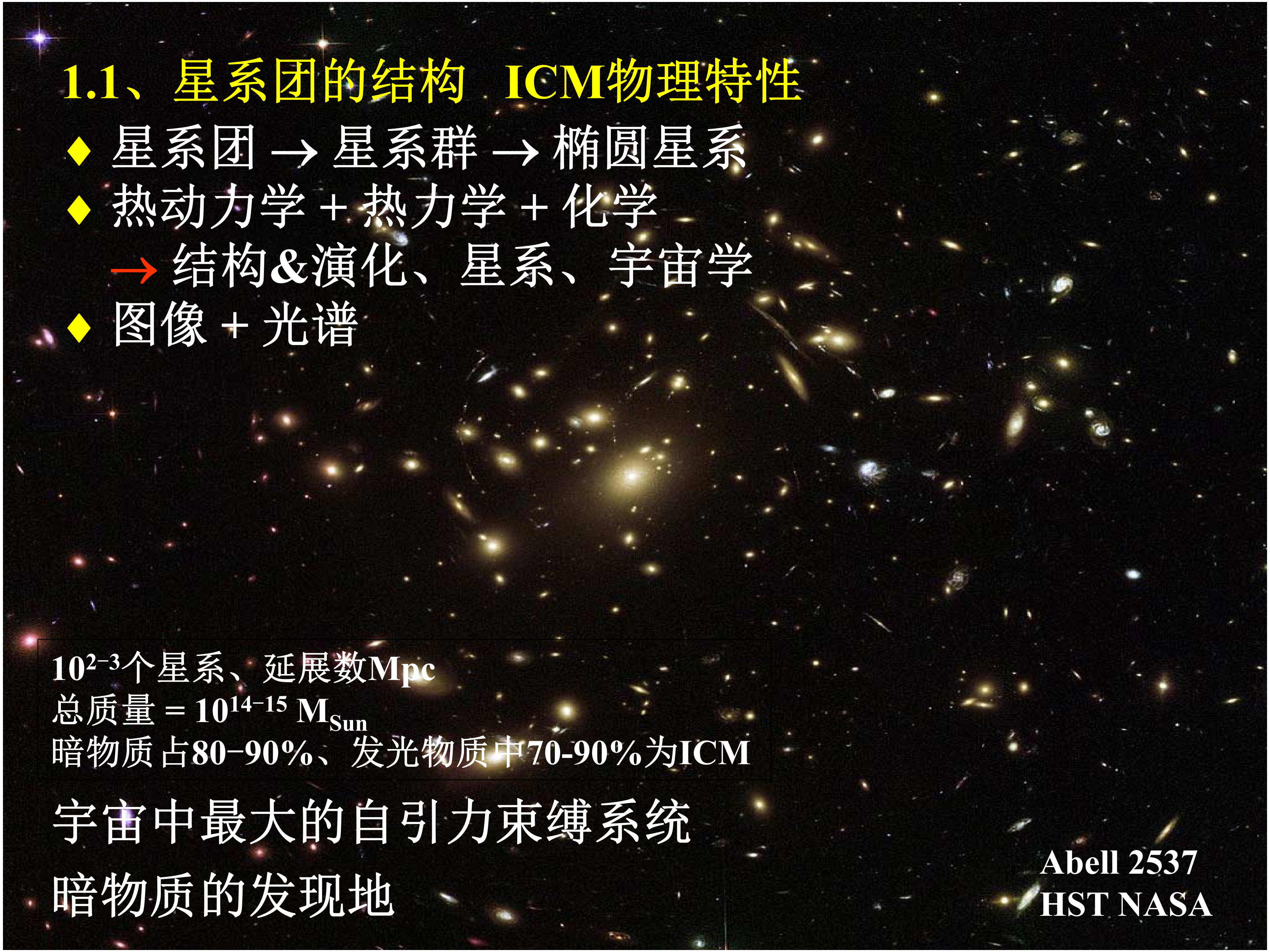

10^{2-3}个星系、延展数Mpc
总质量 = 10^{14-15} M_{Sun}
暗物质占80−90%、发光物质中70-90%为ICM

宇宙中最大的自引力束缚系统
暗物质的发现地

Abell 2537
HST NASA

♦ 星系团大量存在于宇宙大尺度纤维状结构上

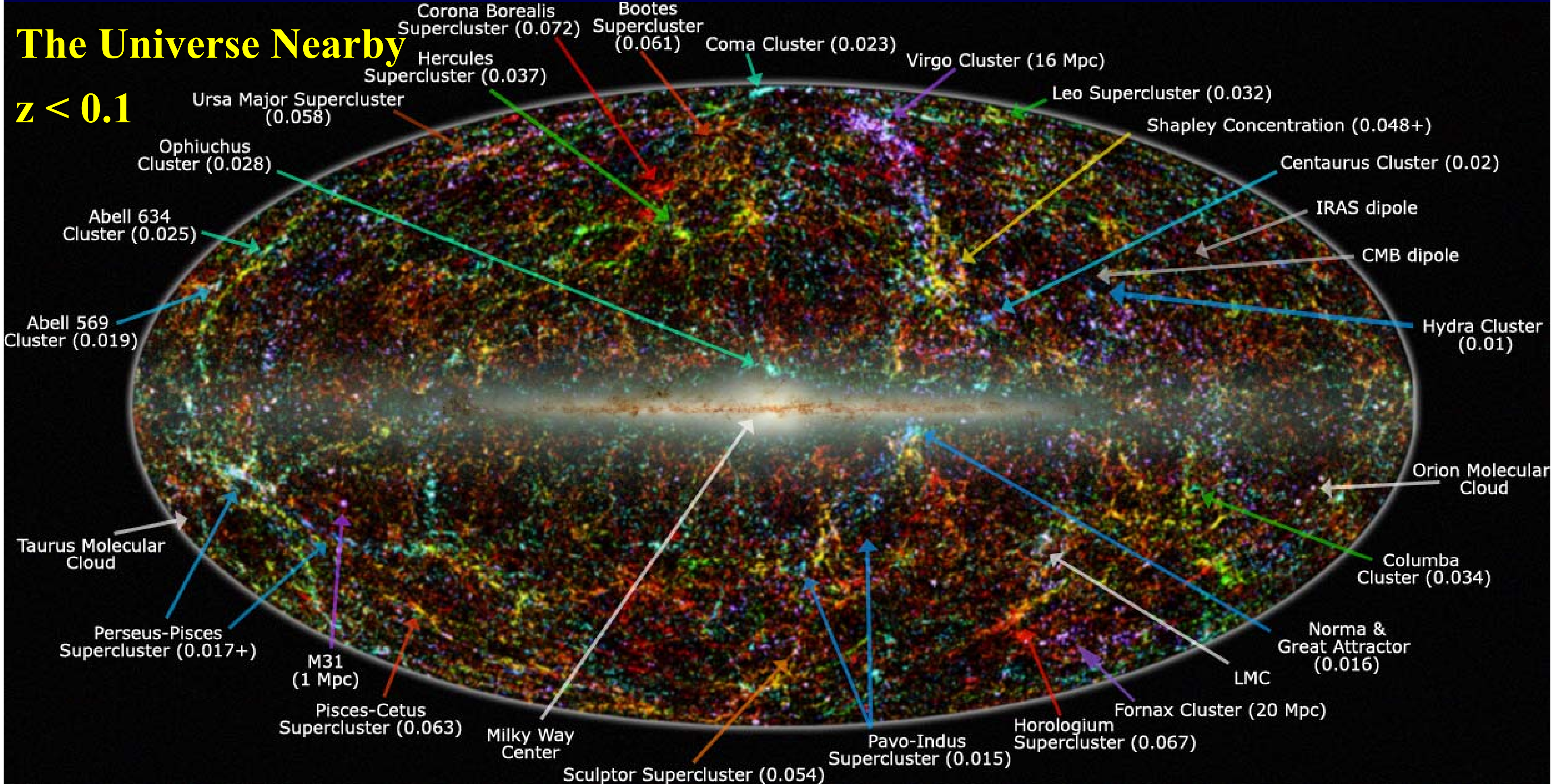

近红外天空中的150万个星系和5000万颗恒星

XSC（the 2MASS Extended Source Catalog） Jarrett 2004

◆ 光学 + X射线 + 射电

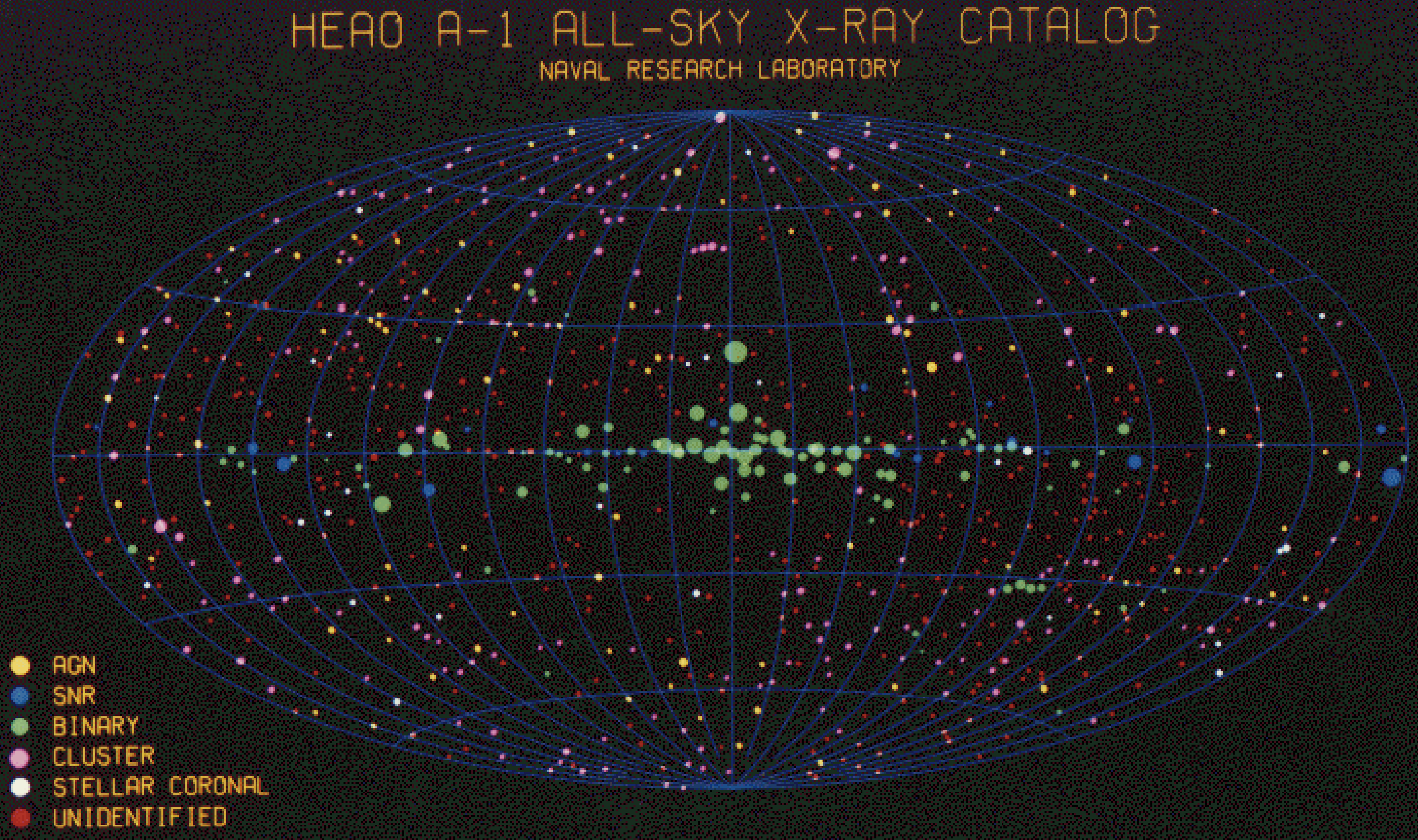

极高温星系际气体的质量 = 3 – 5倍恒星质量

1.2、星系团的演化　并合成长过程

- ◆ 宇宙演化史中重要的角色
- ◆ 与21厘米宇宙学的关联

Discover Magazine

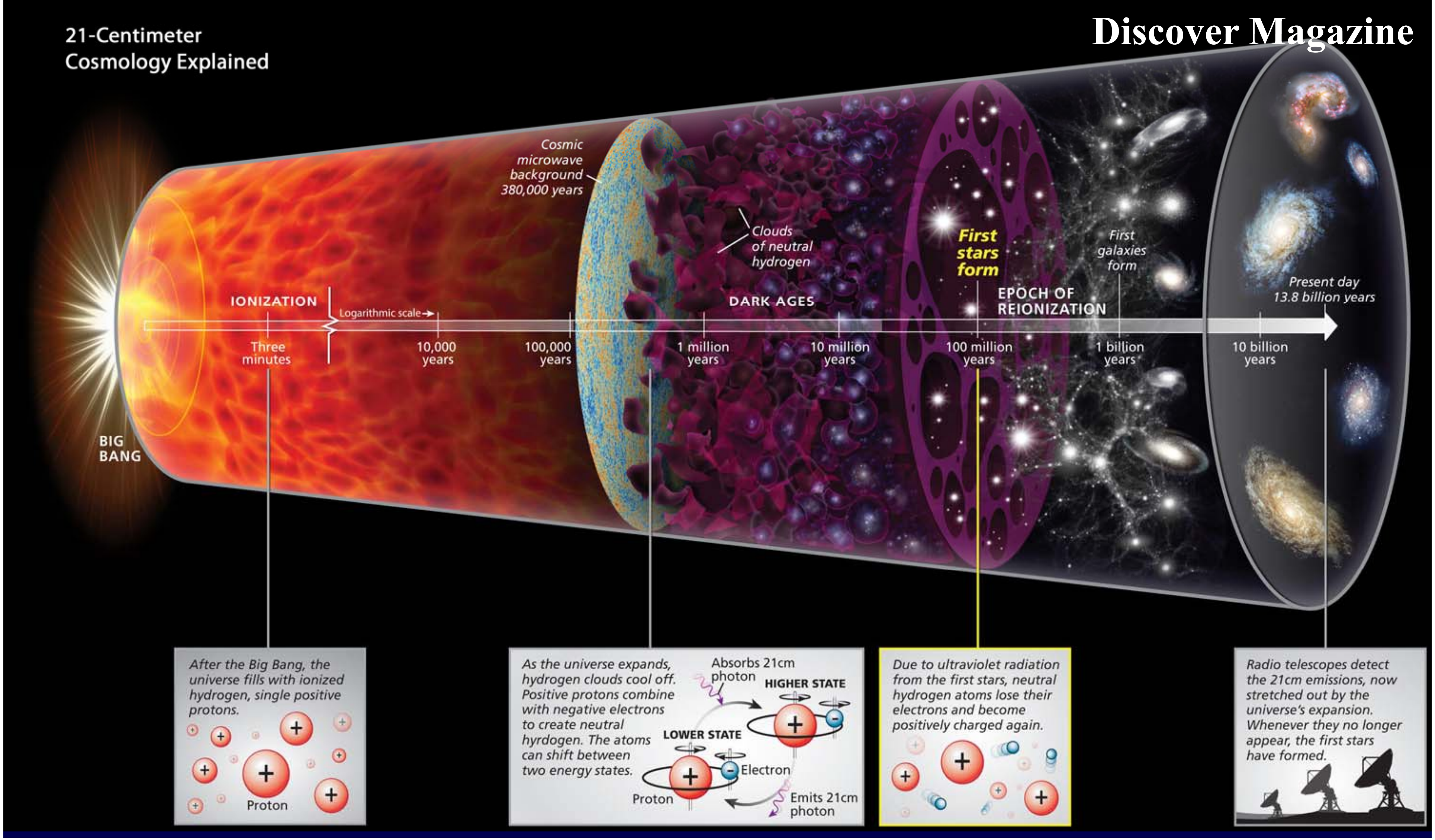

- 冷暗物质（cold dark matter）模型
  等级式成团（hierarchical clustering）模型

  极早期微小密度扰动 →
  CDM 粒子速度弥散很小，
  小尺度结构优先形成 →
  引力+宇宙膨胀作用下
  越来越大尺度的结构形成

- **PS**理论
  PRESS & SCHECHTER 1974
  密度扰动随机统计性 →
  单位共动体积内暗晕数目
  随质量的分布

$$n_{\rm cl}(M,z)\,{\rm d}M=\sqrt{\frac{2}{\pi}}\frac{\langle\rho_0\rangle}{M}\frac{\delta_c(z)}{\sigma^2(M)}\left|\frac{{\rm d}\sigma(M)}{{\rm d}M}\right|\exp\left[-\frac{\delta_c^2(z)}{2\sigma^2(M)}\right]{\rm d}M, \qquad (4\text{–}1)$$

其中 M 是星系团的质量，$\langle\rho_0\rangle$ 是当前的宇宙平均密度，$\delta_c(z)$ 是暗物质坍缩形成暗物质晕的临界线性过密度 (critical linear overdensity) [参见式 (A–11)]，$\sigma(M)$ 是当前在平均质量为 M 的球形区域里的密度涨落方均根值。

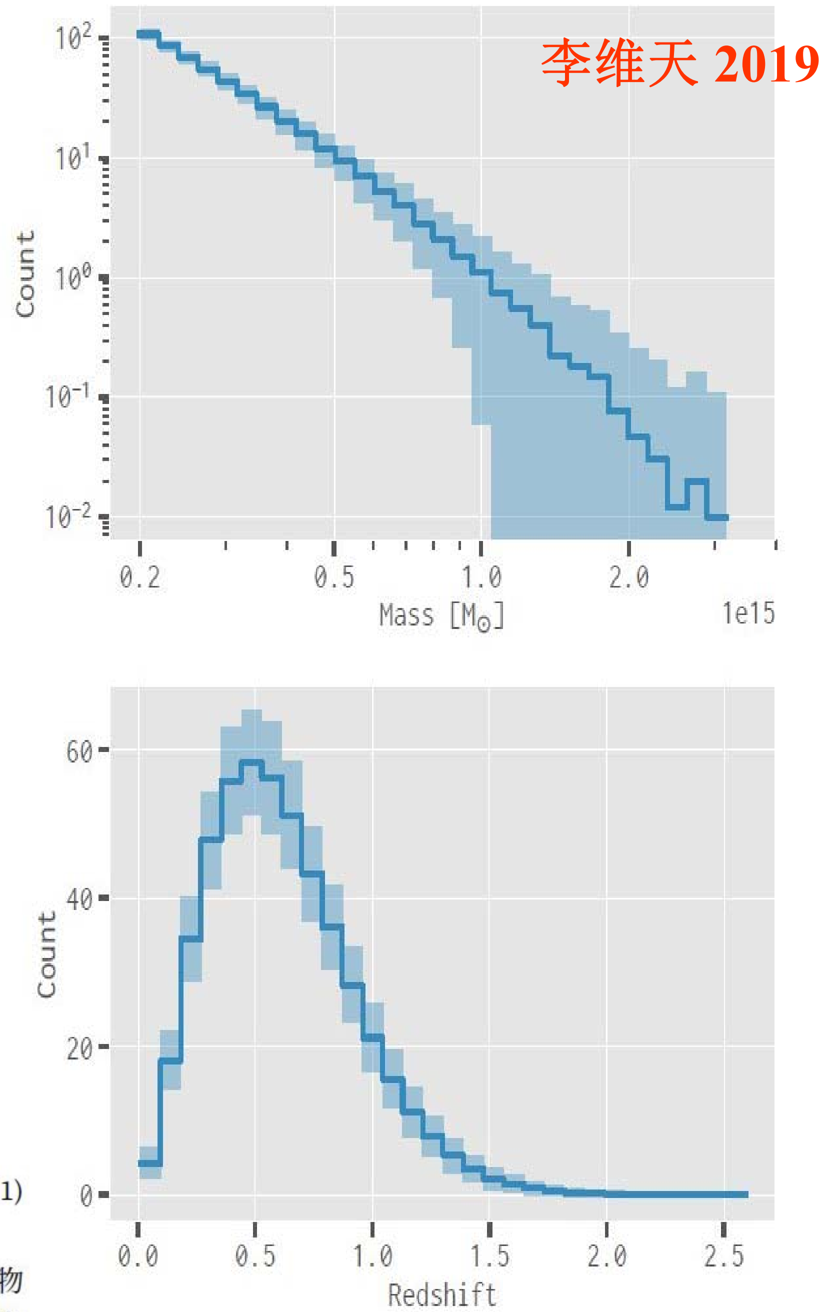

$10^\circ\times10^\circ$ 的天区内，星系团的质量（上栏）和红移（下栏）分布直方图。图中的实线和阴影区域分别表示 500 次模拟的平均值和 68% 的误差。

- 扩展PS 理论
  多种Monte Carlo算法用于构建星系团成长（并合树）

  LACEY & COLE 1993算法
  较简洁、常用
  （二叉树、简单质量求和）

  吸积 + 并合（$\Delta M_c = 10^{13}\ M_{sun}$）

设一个星系团在 t_1 时刻的质量为 M_1，经过一次成长步骤（并合或吸积）后，其质量在 t_2 ($> t_1$) 时刻增长为 M_2。给定 M_2 和 t_2，扩展 PS 理论给出了该星系团在一个较早时刻 t_1 具有一个质量范围为 $[M_1, M_1 + \mathrm{d}M_1]$ 的前身的条件概率 (conditional probability) 为[266, 268]：

$$\Pr(M_1, t_1 \,|\, M_2, t_2)\,\mathrm{d}M_1 = \frac{1}{\sqrt{2\pi}}\frac{M_2}{M_1}\frac{\delta_{c1}-\delta_{c2}}{(\sigma_1^2-\sigma_2^2)^{3/2}}\left|\frac{\mathrm{d}\sigma_1^2}{\mathrm{d}M_1}\right|\exp\left[-\frac{(\delta_{c1}-\delta_{c2})^2}{2(\sigma_1^2-\sigma_2^2)}\right]\mathrm{d}M_1, \tag{4–4}$$

其中 $\delta_{ci} \equiv \delta_c(t_i)$，$\sigma_i \equiv \sigma(M_i)$，同时下标 $i = 1, 2$ 分别表示这两个参数在时刻 t_1 和 t_2 的值。进一步定义 $\psi \equiv \sigma^2(M)$ 和 $\omega \equiv \delta_c(t)$，上式可简化为：

$$\Pr(\Delta\psi, \Delta\omega)\,\mathrm{d}\Delta\psi = \frac{1}{\sqrt{2\pi}}\frac{\Delta\omega}{(\Delta\psi)^{3/2}}\exp\left[-\frac{(\Delta\omega)^2}{2\Delta\psi}\right]\mathrm{d}\Delta\psi, \tag{4–5}$$

其中 $\Delta\psi = \sigma_1^2 - \sigma_2^2$，$\Delta\omega = \delta_{c1} - \delta_{c2}$。注意，$\psi$ 随 M 的增大而单调递减，ω 也随 t 的增大而单调递减。

为了模拟一个星系团的并合树，从该星系团的“当前”质量 M_{sim} 和红移 z_{sim} 出发，运用 Monte Carlo 方法逐步追溯其成长历史，追溯的时间步长为 $\Delta\omega$。为了能够分辨质量变化为 ΔM_c ($\ll M_2$) 的并合，时间步长 $\Delta\omega$ 应满足[268]：

$$\Delta\omega \lesssim (\Delta\omega)_{\max} = \left[\psi\left|\frac{\mathrm{d}\ln\sigma^2}{\mathrm{d}\ln M_2}\right|\left(\frac{\Delta M_c}{M_2}\right)\right]^{1/2} \tag{4–6}$$

李维天 2019

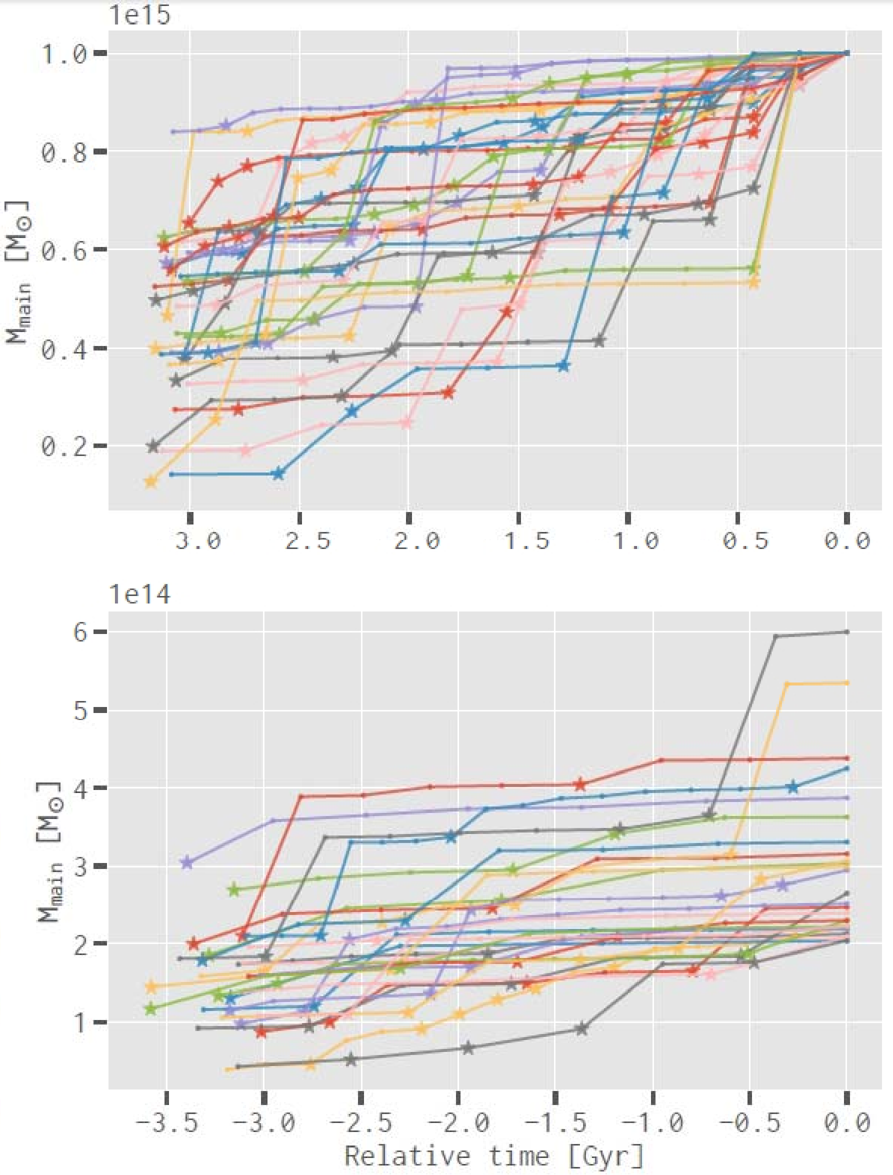

Figure 2. (**Upper**) Merger trees for one galaxy cluster of mass $10^{15}\ M_\odot$ obtained by repeating the random build process for 30 times. (**Lower**) Example merger trees for 30 galaxy clusters randomly drawn from the sample constructed in Section 2.1.1. Asterisks mark merger events and dots represent accretion events.

Li et al. 2019 ApJ

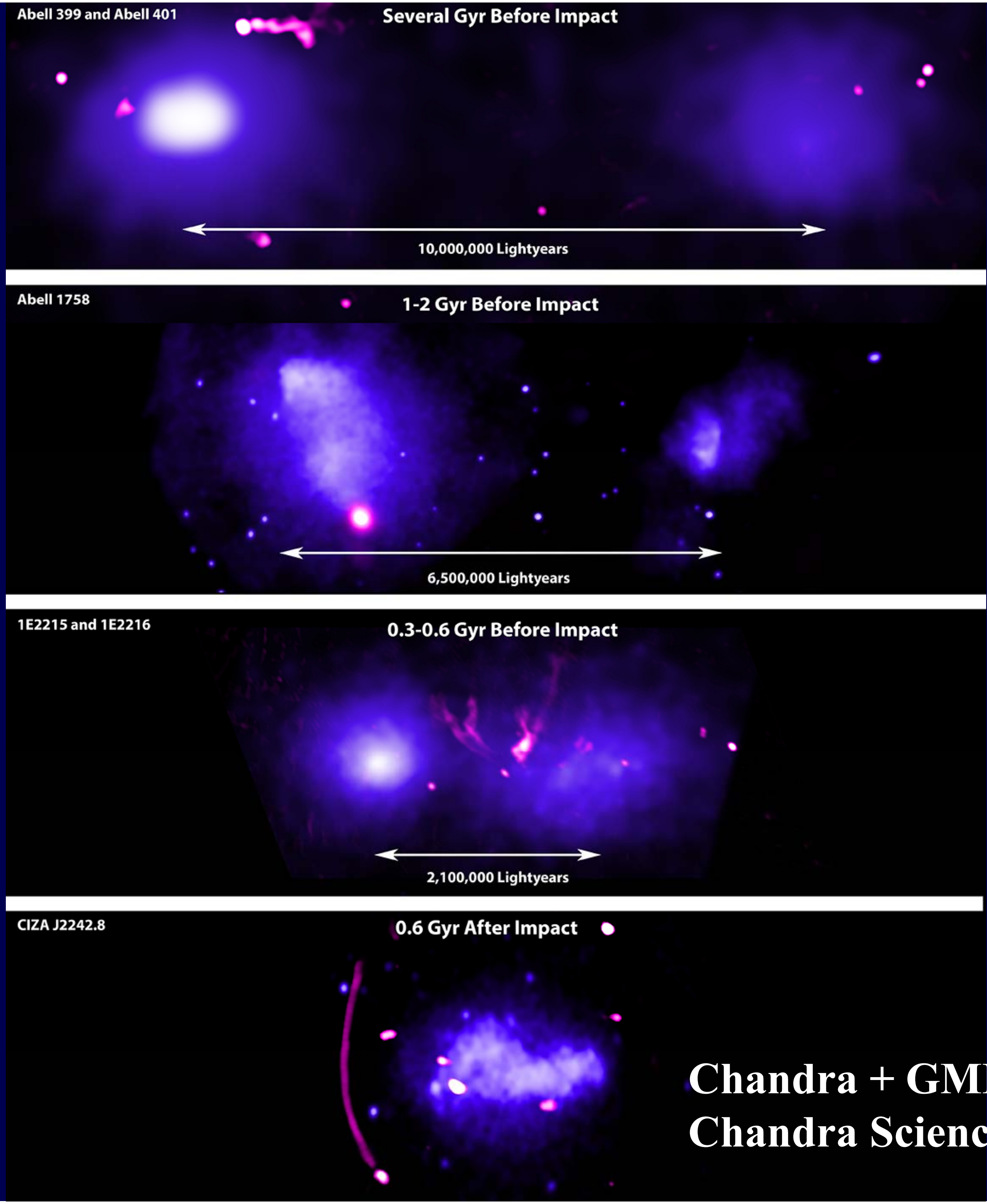

Chandra + GMRT
Chandra Science Center

1.3、研究内容、现有成果及其意义

- 热动力学物理（激波、冷锋、KHI、暗物质等等）
  化学演化（恒星形成、超新星核合成、扩散机制）
- 超大质量黑洞/活动星系核（AGN）与ICM间的作用
- 星系团并合、大尺度宏观运动

- 极端条件下的天然物理实验室
- 星系-宇宙大尺度结构间的桥梁
  → 独立的宇宙学探针
- 强调多波段仪器间的协作

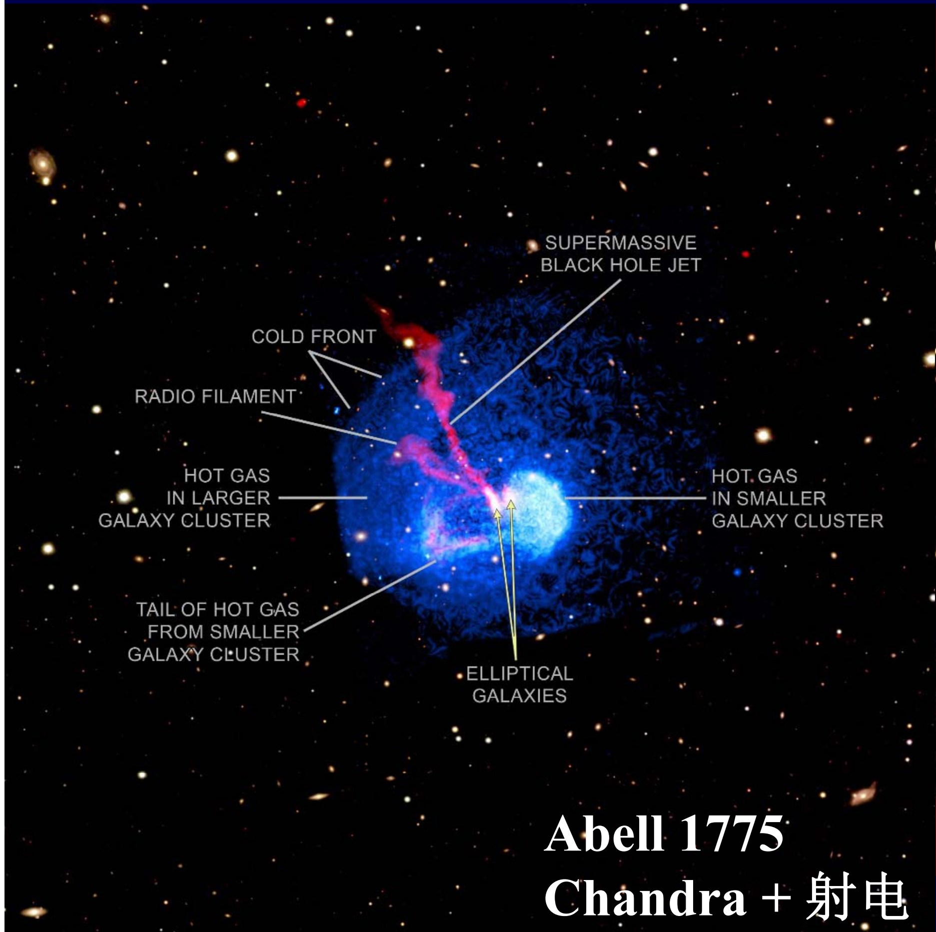

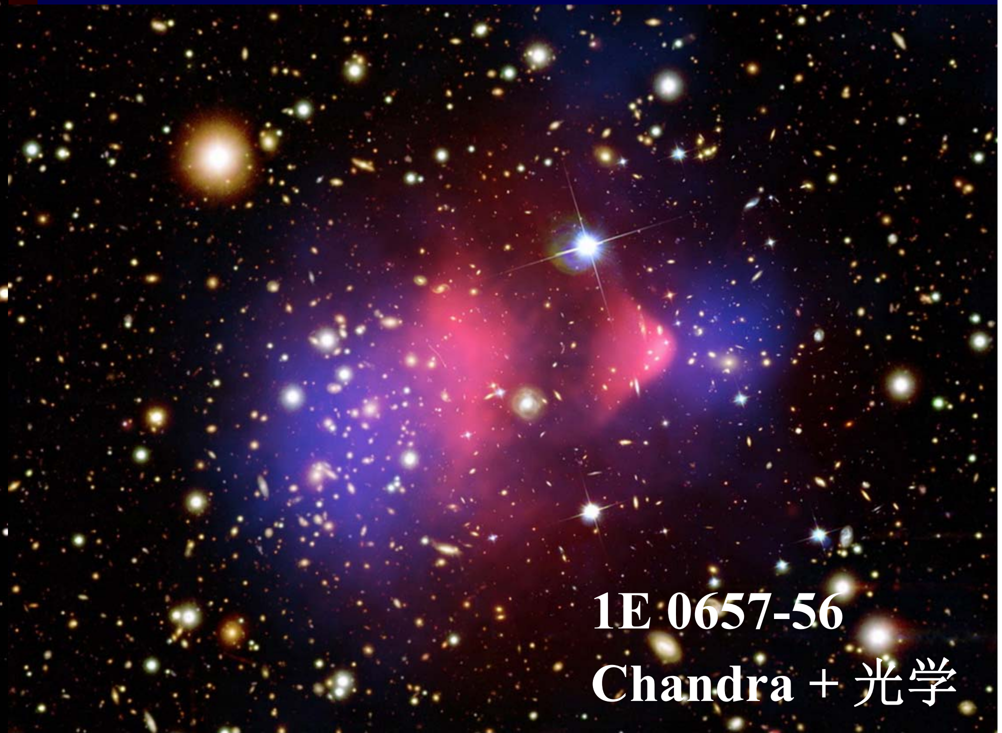

NASA HEASARC

2、AGN活动对星系团的影响I：较传统话题

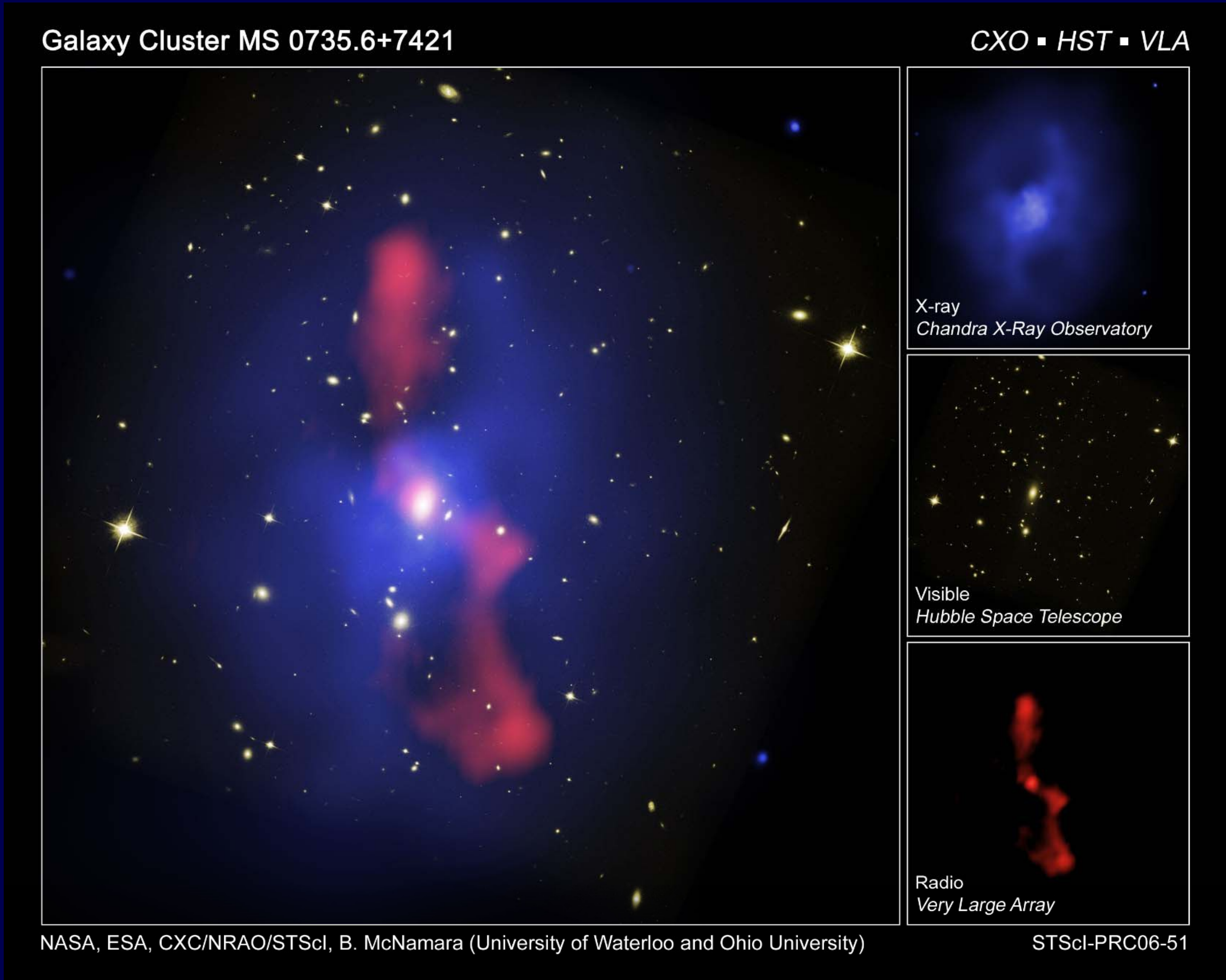

2.1、问题的提出：围绕冷流模型的疑问

◆ ICM的温度及其分布　◆ 气体冷却时间

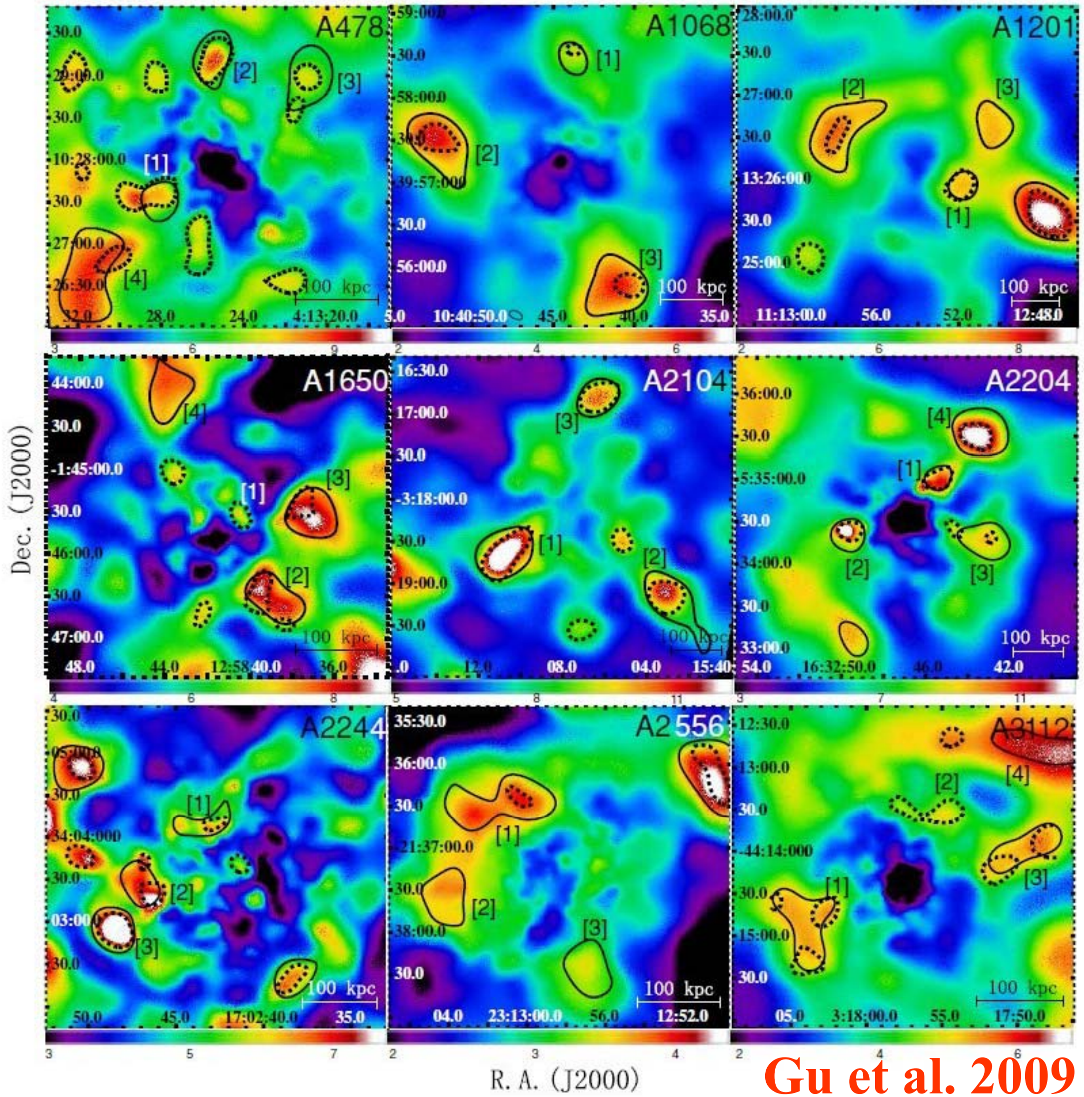

Gu et al. 2009 ApJ

Figure 4. Projected temperature maps, on which the most significant substructures with the characteristic scales indicated by the wavelet spectra (Figure 5), i.e., $i = 7$ (100–200 h_{70}^{-1} kpc; solid line) and $i = 6$ (50–100 h_{70}^{-1} kpc; dotted line) are marked (Section 3.3.2). The representative substructures are labeled with the same numbers as used in Table 4.

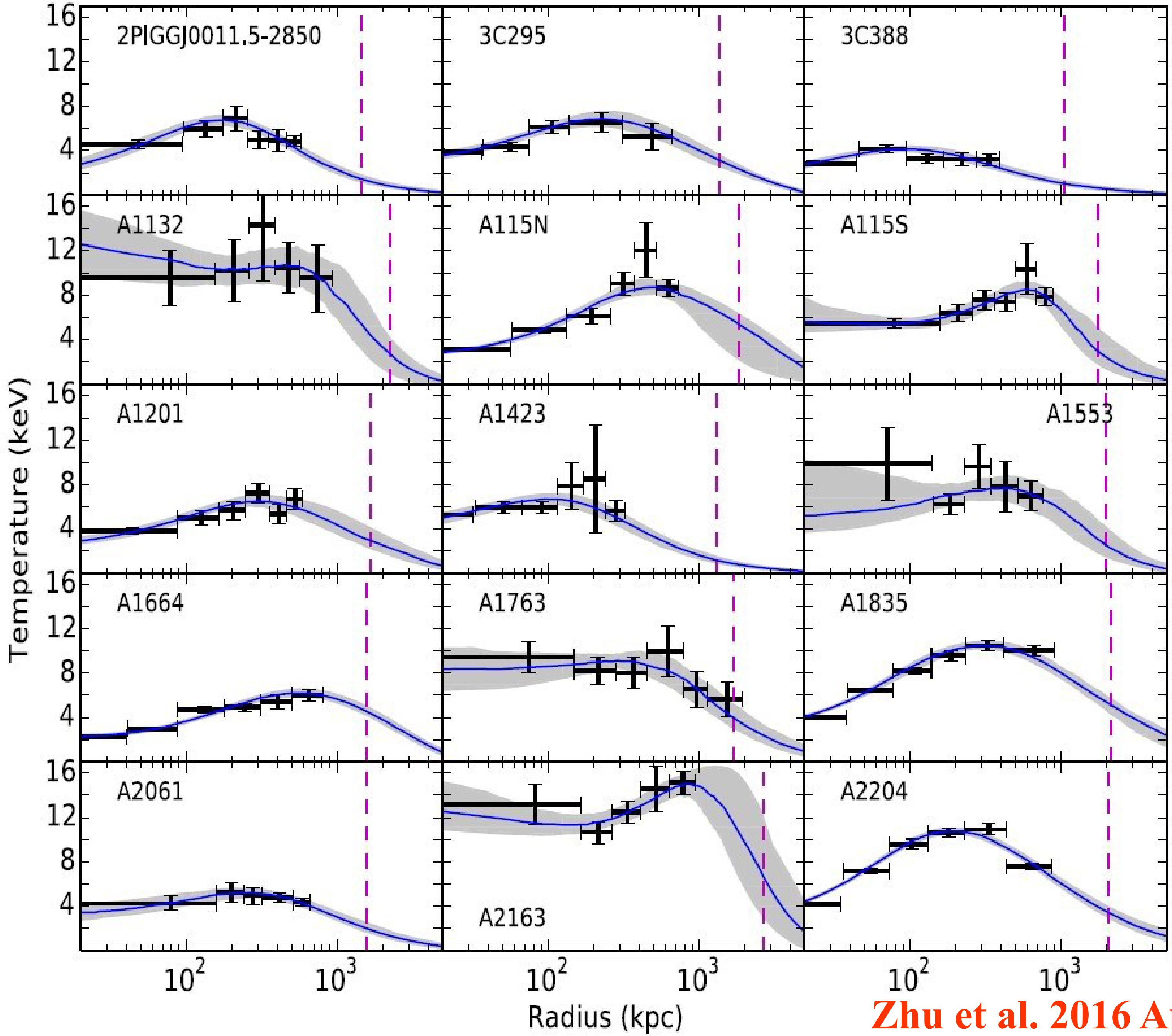

Zhu et al. 2016 ApJ

Figure 1. Best-fit gas temperature profiles that were obtained with our model (dark blue curves) along with the 68% errors (shadow) and the *Chandra* measurements (black crosses) after the projection effect was corrected (Section 3.2). The vertical dashed lines indicate $1.5r_{500}$ of each cluster.

- 中央区域气体冷却过快的问题（冷却半径）
- 冷流 → 冷核

Table 3
Classifications of Sample Clusters with Both the Three Traditional Diagnostics (Coincidentally) and the New CC Diagnostic

Name[a]	$t_{\rm cool}$[b] ($h_{71}^{-1/2}$ Gyr)	α[c]	$C_{\rm SB}$[d]	$r_{\rm cool}$[e] (kpc)	$\Delta_{\rm PE}$[f]	$R_{\rm excess}$[g] (%)	Category[h]
A0193	$12.22^{+2.27}_{-2.31}$	$0.23^{+0.03}_{-0.01}$	$0.047^{+0.003}_{-0.002}$	$14.9^{+9.1}_{-6.4}$	0.24 ± 0.03	1.9 ± 0.5	NCC/NCC
A0520	$8.04^{+2.21}_{-2.22}$	$0.03^{+0.00}_{-0.00}$	$0.016^{+0.003}_{-0.002}$	⋯	0.27 ± 0.04	⋯	NCC/NCC
A0697	$11.04^{+3.02}_{-4.62}$	$0.20^{+0.02}_{-0.03}$	$0.035^{+0.002}_{-0.003}$	⋯	0.17 ± 0.05	⋯	NCC/NCC
A0795	$3.87^{+0.42}_{-0.74}$	$0.68^{+0.02}_{-0.04}$	$0.120^{+0.006}_{-0.005}$	$83.6^{+13.5}_{-7.2}$	0.38 ± 0.02	⋯	WCC/WCC
A0963	$2.32^{+0.27}_{-0.29}$	$0.52^{+0.03}_{-0.03}$	$0.098^{+0.005}_{-0.005}$	$88.1^{+12.2}_{-9.9}$	0.36 ± 0.02	1.7 ± 0.2	WCC/WCC
A0970	$15.45^{+3.47}_{-4.44}$	$0.20^{+0.03}_{-0.02}$	$0.041^{+0.003}_{-0.003}$	⋯	0.26 ± 0.06	⋯	NCC/NCC
A1068	$0.91^{+0.06}_{-0.07}$	$1.09^{+0.03}_{-0.04}$	$0.281^{+0.011}_{-0.010}$	$109.4^{+4.4}_{-5.3}$	0.56 ± 0.01	45.7 ± 21.9	SCC/SCC
A1204	$0.75^{+0.07}_{-0.08}$	$1.12^{+0.02}_{-0.04}$	$0.328^{+0.013}_{-0.013}$	$111.6^{+8.0}_{-5.4}$	0.43 ± 0.02	⋯	SCC/SCC
A1651	$3.06^{+0.60}_{-0.60}$	$0.70^{+0.05}_{-0.06}$	$0.076^{+0.004}_{-0.004}$	$66.8^{+18.9}_{-14.7}$	0.34 ± 0.03	10.2 ± 1.7	WCC/WCC
A1664	$0.99^{+0.06}_{-0.07}$	$1.14^{+0.03}_{-0.04}$	$0.209^{+0.008}_{-0.008}$	$93.4^{+3.8}_{-3.6}$	0.52 ± 0.01	15.3 ± 2.7	SCC/SCC
A1736	$24.62^{+6.50}_{-10.89}$	$0.15^{+0.01}_{-0.03}$	$0.022^{+0.002}_{-0.002}$	⋯	0.22 ± 0.08	1.2 ± 0.3	NCC/NCC
A1991	$0.67^{+0.01}_{-0.02}$	$1.16^{+0.01}_{-0.03}$	$0.204^{+0.007}_{-0.007}$	$67.3^{+1.4}_{-1.3}$	0.56 ± 0.01	50.4 ± 11.7	SCC/SCC
A2034	$19.79^{+2.97}_{-3.09}$	$0.12^{+0.01}_{-0.00}$	$0.030^{+0.001}_{-0.002}$	⋯	0.25 ± 0.02	0.3 ± 0.0	NCC/NCC
A2061	$27.75^{+10.82}_{-11.16}$	$0.03^{+0.01}_{-0.01}$	$0.016^{+0.002}_{-0.002}$	⋯	0.16 ± 0.09	⋯	NCC/NCC
A2104	$27.77^{+4.58}_{-5.75}$	$0.12^{+0.00}_{-0.00}$	$0.040^{+0.002}_{-0.002}$	$9.5^{+8.1}_{-9.5}$	0.26 ± 0.03	0.5 ± 0.1	NCC/NCC
A2163	$14.36^{+1.25}_{-2.04}$	$0.15^{+0.01}_{-0.01}$	$0.023^{+0.001}_{-0.001}$	⋯	0.23 ± 0.02	⋯	NCC/NCC
A2255	$28.27^{+3.81}_{-6.21}$	$0.09^{+0.01}_{-0.01}$	$0.019^{+0.001}_{-0.001}$	⋯	0.18 ± 0.06	⋯	NCC/NCC
A2319	$13.40^{+1.39}_{-4.11}$	$0.46^{+0.02}_{-0.07}$	$0.043^{+0.002}_{-0.002}$	⋯	0.35 ± 0.04	0.8 ± 0.1	NCC/WCC
A2443	$14.51^{+5.54}_{-6.38}$	$0.16^{+0.02}_{-0.01}$	$0.043^{+0.003}_{-0.003}$	⋯	0.24 ± 0.04	⋯	NCC/NCC
A2554	$11.87^{+2.20}_{-3.12}$	$0.20^{+0.01}_{-0.01}$	$0.066^{+0.004}_{-0.004}$	⋯	0.21 ± 0.03	1.1 ± 0.3	NCC/NCC
A2657	$3.33^{+0.84}_{-0.79}$	$0.61^{+0.12}_{-0.11}$	$0.077^{+0.004}_{-0.003}$	$38.2^{+14.9}_{-12.6}$	0.35 ± 0.03	1.0 ± 0.1	WCC/WCC
A2667	$1.20^{+0.18}_{-0.18}$	$0.54^{+0.03}_{-0.04}$	$0.152^{+0.007}_{-0.008}$	$135.9^{+14.2}_{-12.9}$	0.47 ± 0.02	4.5 ± 0.5	WCC/SCC
A3158	$11.27^{+1.28}_{-1.54}$	$0.29^{+0.02}_{-0.01}$	$0.041^{+0.002}_{-0.002}$	$24.8^{+7.0}_{-3.9}$	0.25 ± 0.02	0.1 ± 0.0	NCC/NCC
A3364	$13.19^{+3.77}_{-5.65}$	$0.14^{+0.01}_{-0.01}$	$0.040^{+0.003}_{-0.004}$	$13.5^{+46.4}_{-13.5}$	0.17 ± 0.04	⋯	NCC/NCC
A3376	$9.44^{+1.10}_{-0.94}$	$0.27^{+0.01}_{-0.01}$	$0.027^{+0.002}_{-0.002}$	⋯	0.29 ± 0.03	⋯	NCC/NCC
A3391	$24.47^{+6.87}_{-7.37}$	$0.14^{+0.01}_{-0.01}$	$0.037^{+0.002}_{-0.002}$	⋯	0.19 ± 0.05	0.7 ± 0.2	NCC/NCC
A3395SW	$20.14^{+2.56}_{-3.74}$	$0.31^{+0.01}_{-0.02}$	$0.039^{+0.002}_{-0.003}$	⋯	0.18 ± 0.04	⋯	NCC/NCC
A3822	$9.56^{+2.21}_{-2.51}$	$0.39^{+0.04}_{-0.03}$	$0.037^{+0.003}_{-0.002}$	$38.9^{+15.1}_{-9.5}$	0.14 ± 0.05	⋯	NCC/NCC
AC114	$10.71^{+1.39}_{-1.68}$	$0.15^{+0.00}_{-0.01}$	$0.034^{+0.002}_{-0.002}$	⋯	0.18 ± 0.04	⋯	NCC/NCC
ESO306-G170B	$2.02^{+0.34}_{-0.26}$	$0.52^{+0.05}_{-0.03}$	$0.125^{+0.006}_{-0.006}$	$45.9^{+6.9}_{-7.5}$	0.40 ± 0.02	20.7 ± 2.7	WCC/WCC
IC1262	$1.15^{+0.08}_{-0.06}$	$0.69^{+0.03}_{-0.02}$	$0.127^{+0.005}_{-0.005}$	$49.1^{+2.0}_{-2.8}$	0.40 ± 0.03	4.9 ± 0.6	WCC/WCC
MACSJ2211.7-0349	$6.28^{+1.39}_{-1.71}$	$0.71^{+0.04}_{-0.04}$	$0.129^{+0.007}_{-0.007}$	$81.7^{+24.1}_{-15.4}$	0.39 ± 0.02	⋯	WCC/WCC
NGC1550	$0.95^{+0.04}_{-0.04}$	$0.97^{+0.03}_{-0.02}$	$0.232^{+0.008}_{-0.008}$	$33.0^{+1.0}_{-1.6}$	0.56 ± 0.06	19.5 ± 3.4	SCC/SCC
PKS0745-19	$1.00^{+0.06}_{-0.07}$	$1.41^{+0.02}_{-0.04}$	$0.204^{+0.008}_{-0.007}$	$104.6^{+5.3}_{-4.1}$	0.56 ± 0.01	13.9 ± 1.0	SCC/SCC
RBS797	$0.86^{+0.10}_{-0.10}$	$1.20^{+0.07}_{-0.07}$	$0.286^{+0.010}_{-0.011}$	$138.1^{+10.0}_{-8.0}$	0.49 ± 0.01	⋯	SCC/SCC
RXCJ1524-3154	$0.88^{+0.06}_{-0.06}$	$1.80^{+0.07}_{-0.06}$	$0.321^{+0.011}_{-0.011}$	$79.1^{+3.2}_{-3.1}$	0.61 ± 0.01	⋯	SCC/SCC
RXCJ2014.8-2430	$0.74^{+0.06}_{-0.05}$	$1.76^{+0.07}_{-0.05}$	$0.296^{+0.011}_{-0.011}$	$104.5^{+5.3}_{-6.1}$	0.63 ± 0.01	37.5 ± 2.0	SCC/SCC
RXJ1423.8 + 2404	$0.87^{+0.08}_{-0.11}$	$1.71^{+0.07}_{-0.12}$	$0.298^{+0.012}_{-0.013}$	$114.6^{+10.7}_{-6.6}$	0.44 ± 0.02	26.1 ± 3.6	SCC/SCC
Zw3146	$0.94^{+0.07}_{-0.06}$	$0.98^{+0.02}_{-0.02}$	$0.207^{+0.008}_{-0.008}$	$143.0^{+5.8}_{-6.9}$	0.55 ± 0.01	7.6 ± 0.5	SCC/SCC
ZwCl0015	$2.91^{+0.32}$[illegible]	$0.61^{+0.03}$[illegible]	$0.082^{+0.005}_{-0.005}$	$49.1^{+7.3}_{-6.0}$	0.25 ± 0.04	4.1 ± 0.7	WCC/NCC
ZwCl2089	[illegible]	[illegible]	$0.308^{+0.013}_{-0.012}$	$113.8^{+10.7}_{-8.7}$	0.53 ± 0.02	23.1 ± 4.4	SCC/SCC

Zhang et al. 2016 ApJ

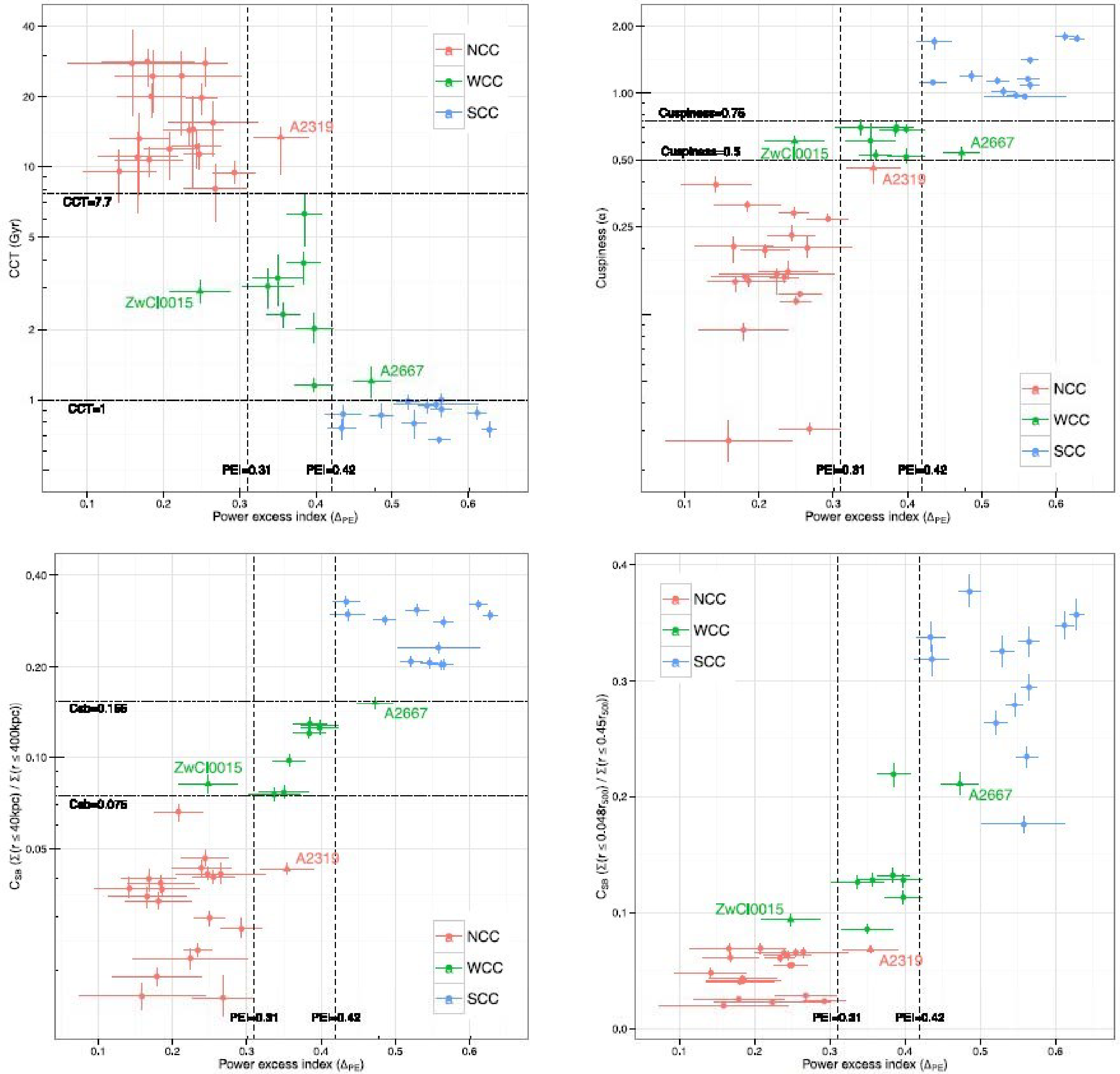

Figure 6. Comparison between the SCC/WCC/NCC classifications derived with the PEI diagnostic and three traditional diagnostics. The relation between the relative core brightness (Section 3.2.5) and the PEI is also plotted (lower right).

♦ 缺乏冷气体的光谱证据

Peterson et al. 2001 A&A
see also Peterson et al. 2003 ApJ

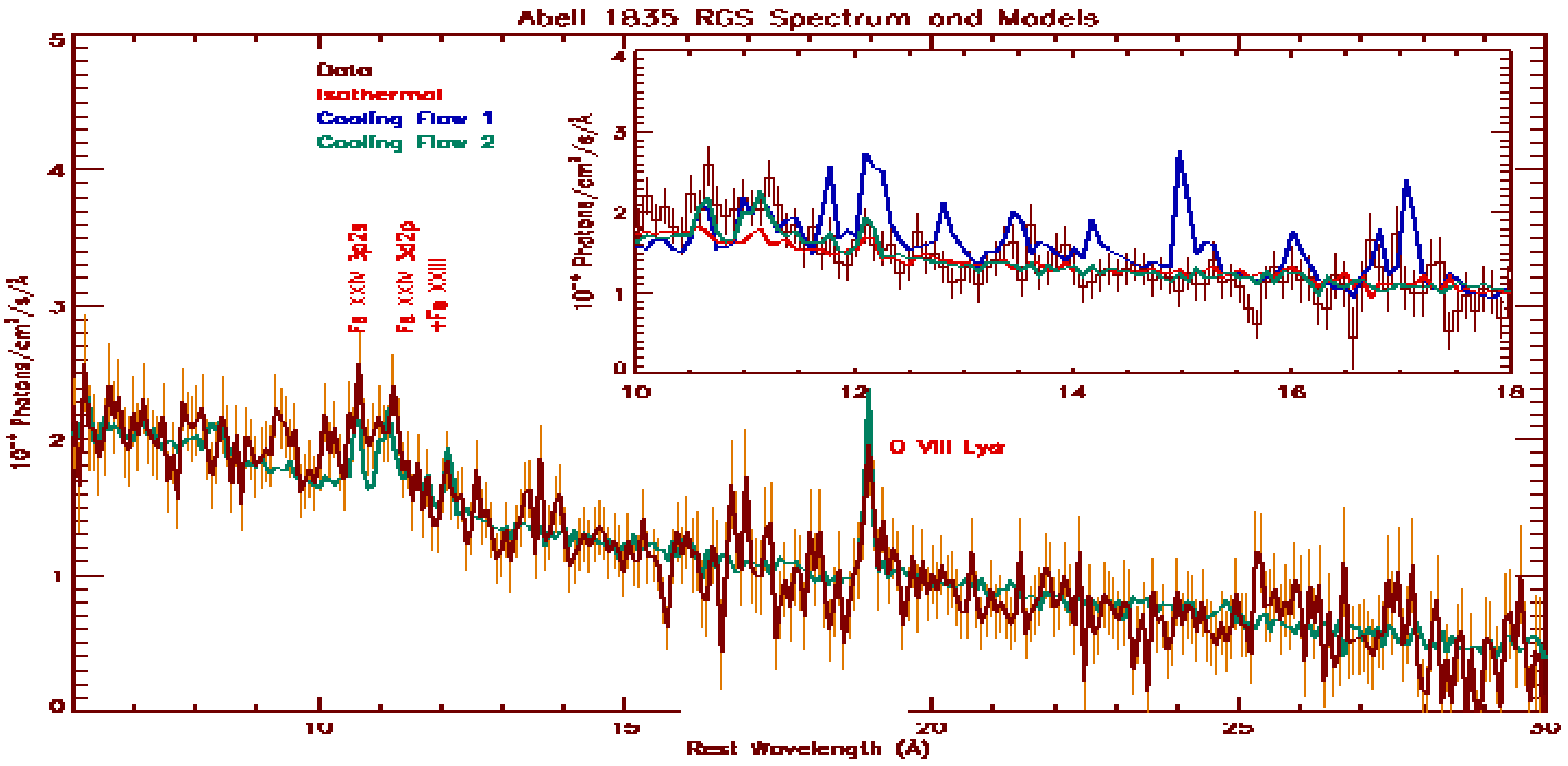

Isothermal model: $kT = 8.2$ keV

CF1: a hot ambient component at 8.2 keV + an isobaric cooling flow component whose lower temperature is $kT_{\rm low} \to 0$.

CF2: Same as CF1 except that $kT_{\rm low} = 2.7$ keV.

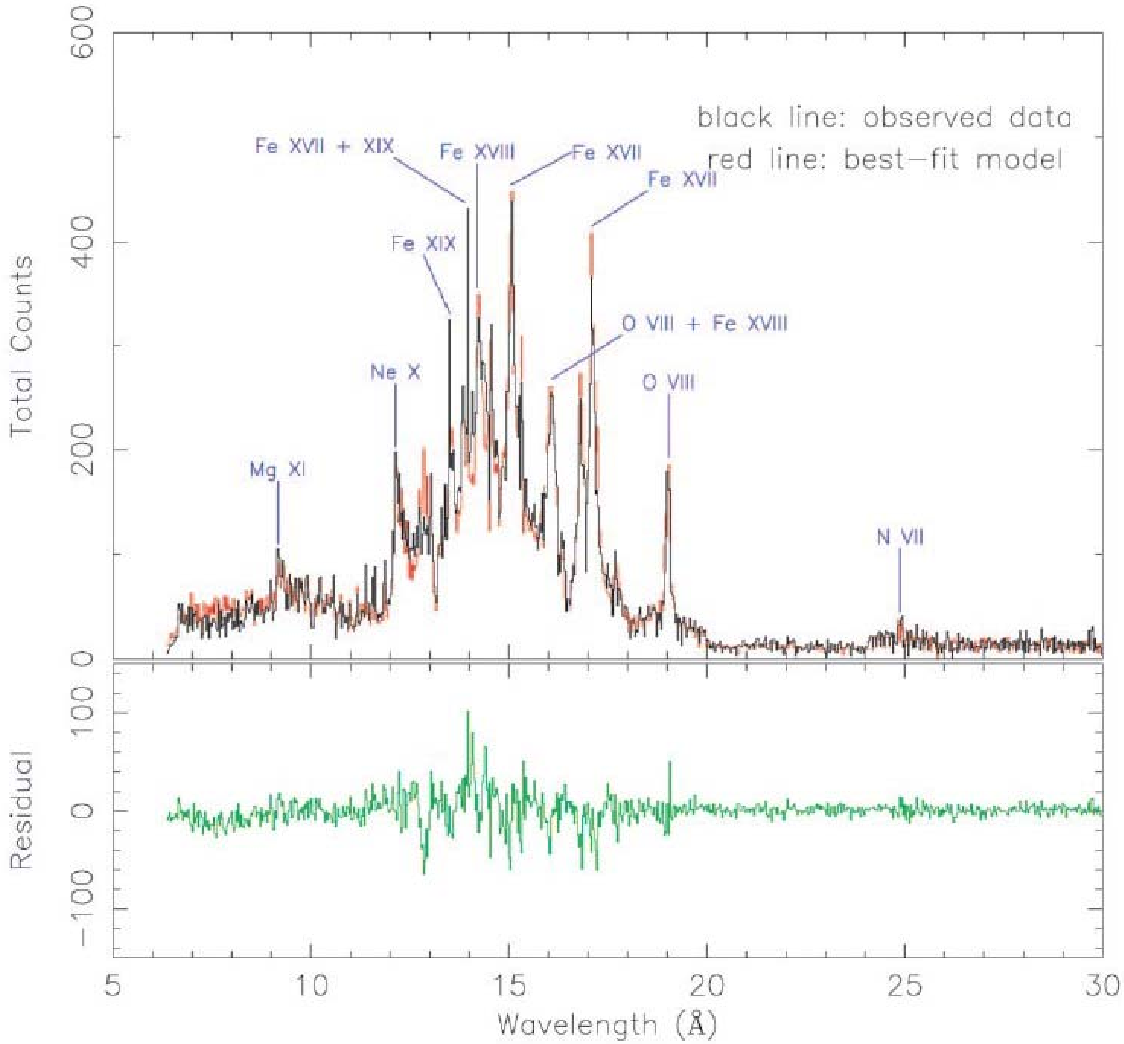

FIG. 1.—Raw, extracted RGS spectrum of NGC 4636 (*black line*), plotted as a function of wavelength. The data from both first and second spectral orders from RGS1 and RGS2 have been added together in constructing this histogram. The best-fit model, allowing for a temperature gradient and accounting for resonance-line scattering effects, is plotted in red. The residuals to the model fit are plotted beneath.

XMM RGS Spectrum of NGC 4636
Xu et al. 2002 ApJ

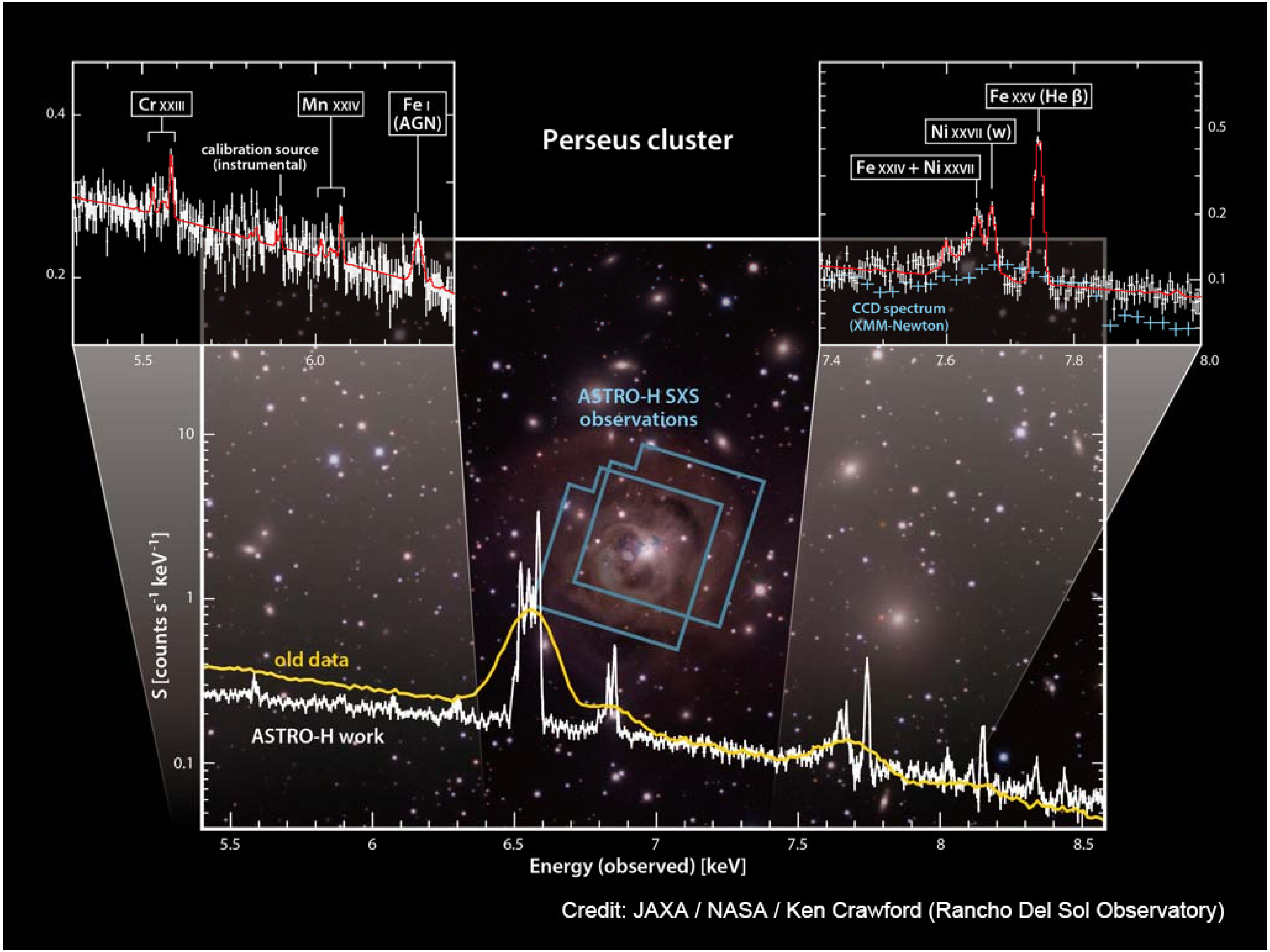

Perseus cluster
Cr XXIII
Mn XXIV
Fe I (AGN)
calibration source (instrumental)
Fe XXV (He β)
Ni XXVII (w)
Fe XXIV + Ni XXVII
CCD spectrum (XMM-Newton)
ASTRO-H SXS observations
old data
ASTRO-H work
S [counts s^{-1} keV^{-1}]
Energy (observed) [keV]
Credit: JAXA / NASA / Ken Crawford (Rancho Del Sol Observatory)

2.2、又一个老问题：金属如何有效扩散？

- 挑战：a. 大量金属遍布ICM各处；b. 外围区的测量及其精度不足；
- 方案：早期增丰（Vigroux 1977年）+ AGN & 并合；
- 需求：以高分辨率光谱识别铁、镁、氧、硅、硫等的空间分布；
- 延伸：a. 建立准确湍流模型；
  b. 以类星体金属吸收线研究星系团外围及其附近大尺度结构

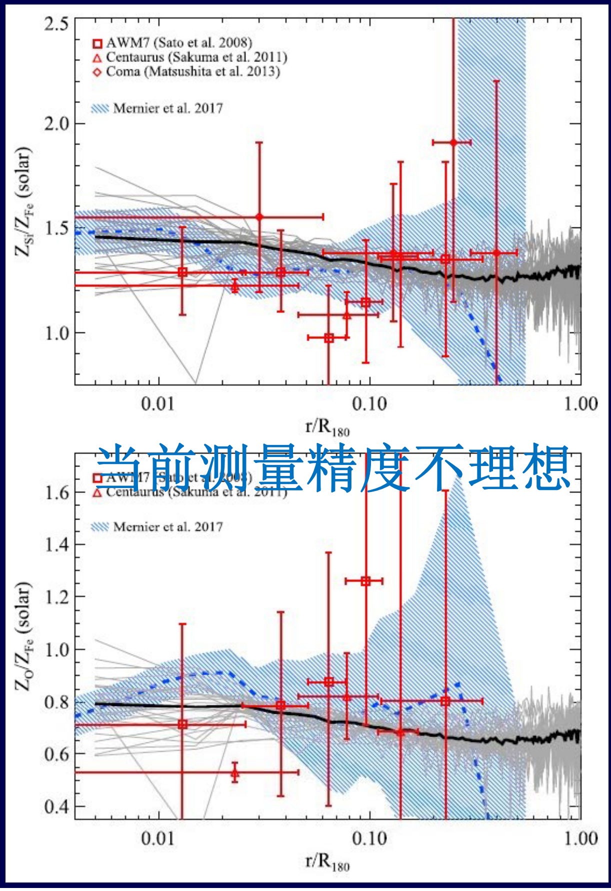

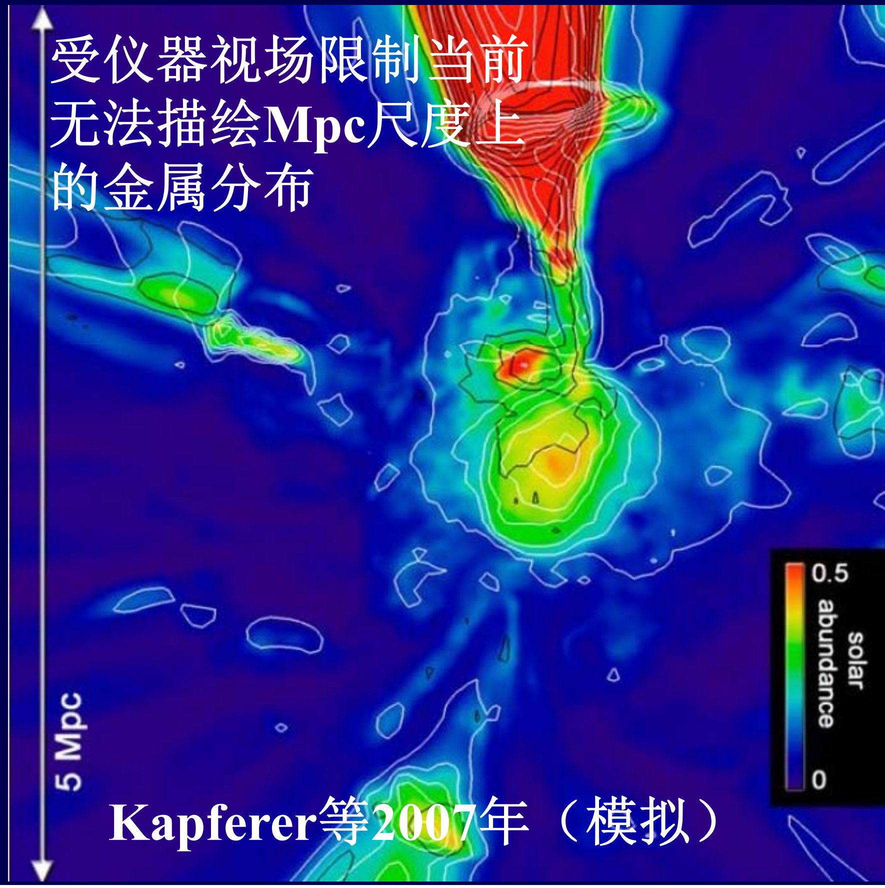

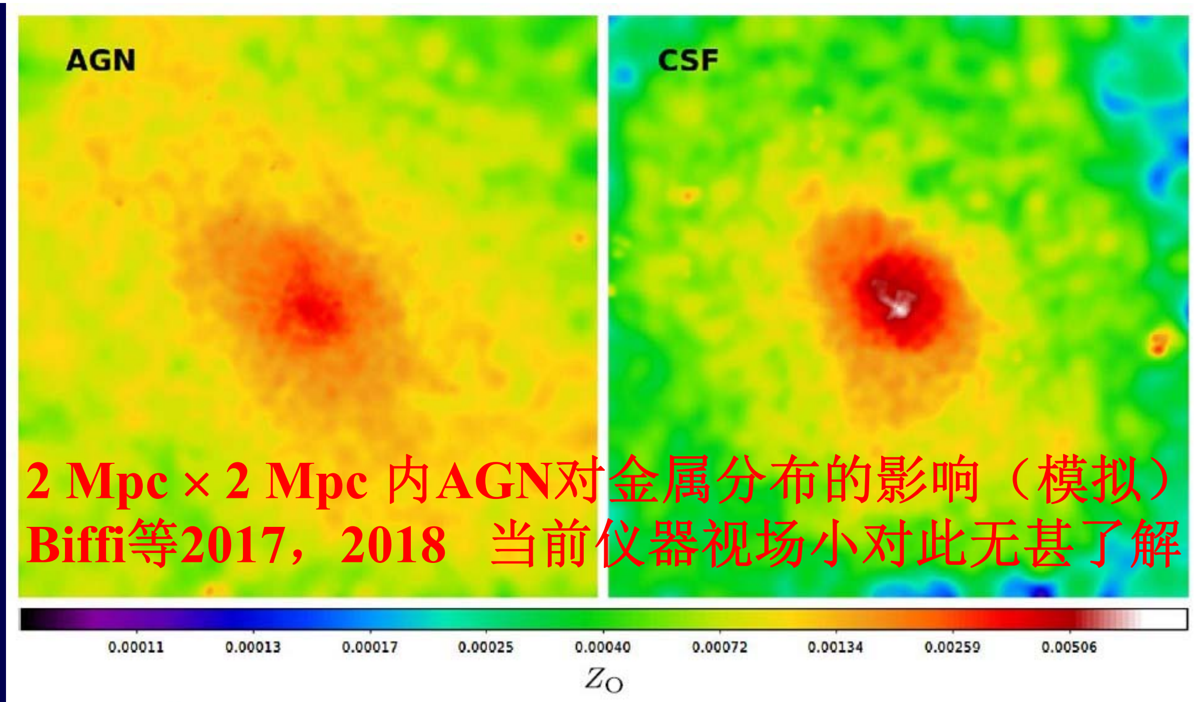

2 Mpc × 2 Mpc 内AGN对金属分布的影响（模拟）
Biffi等2017，2018　当前仪器视场小对此无甚了解

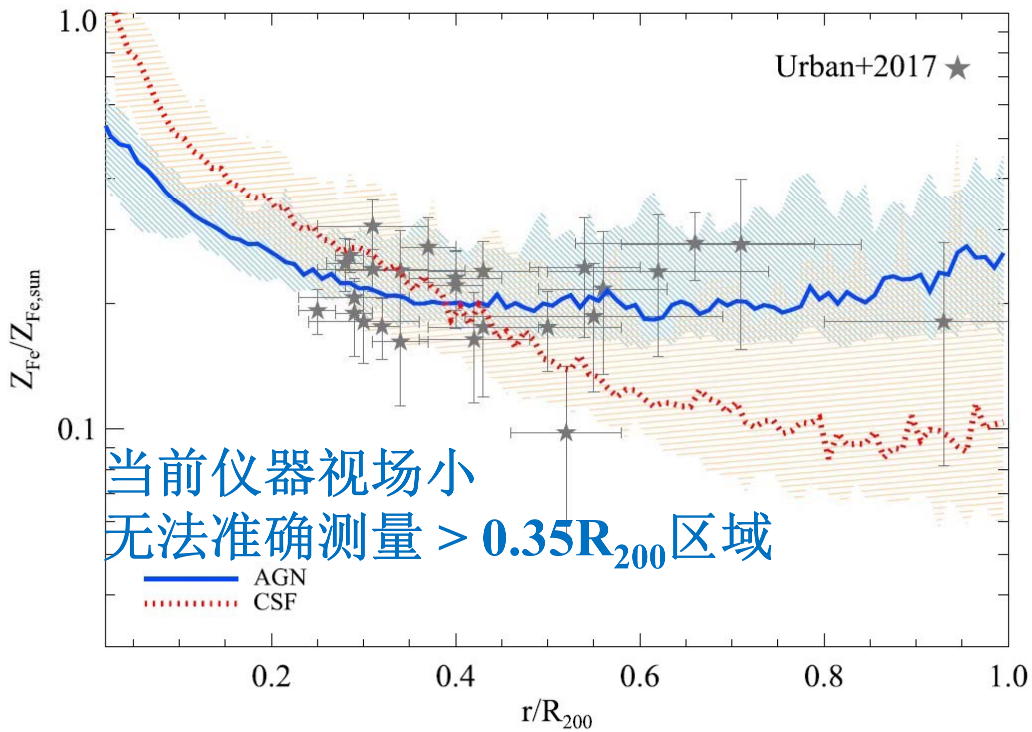

当前仪器视场小
无法准确测量 > $0.35R_{200}$区域

2.3、AGN的角色

◆ AGN活动的形态

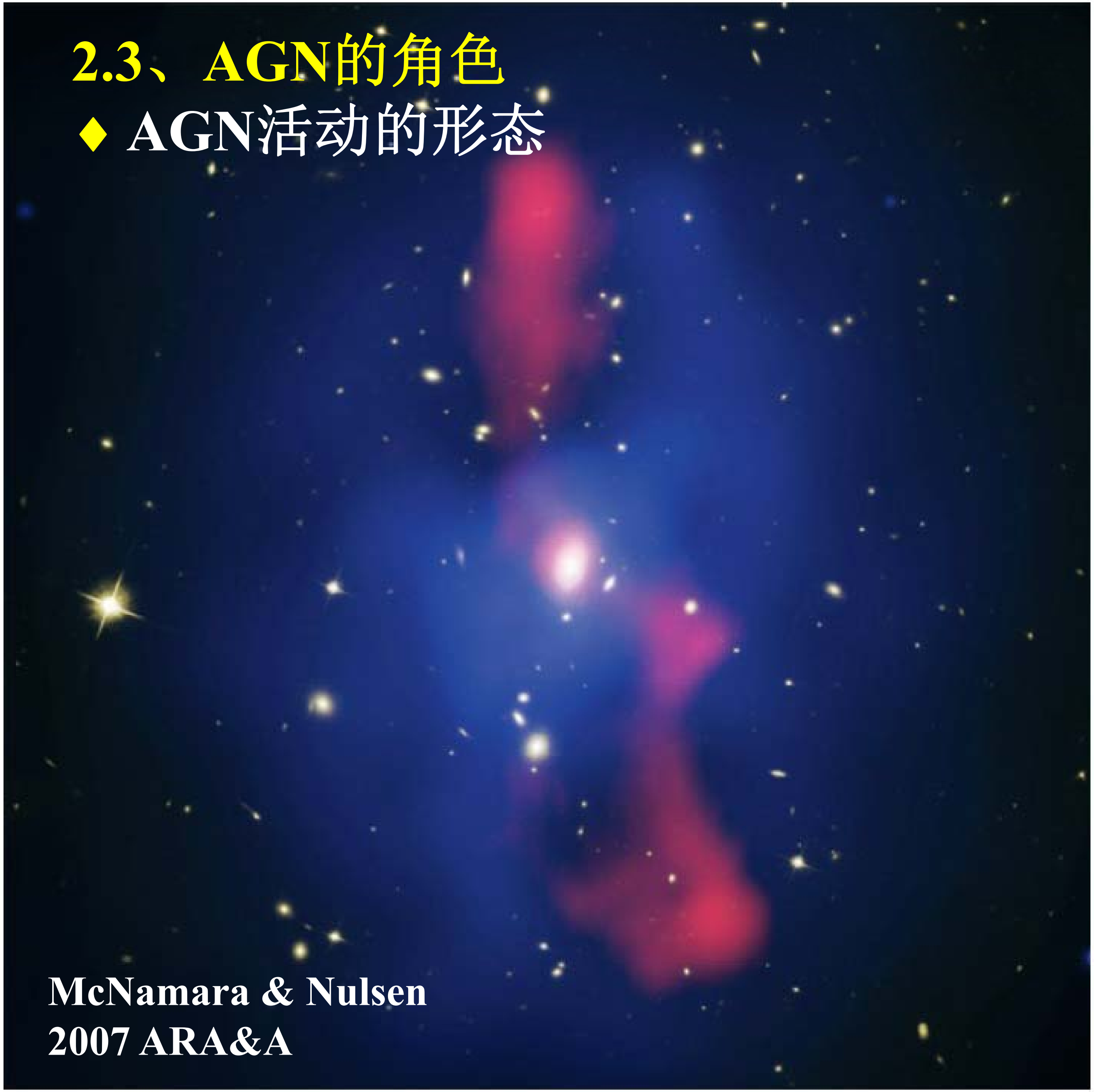

Figure 2

Hubble Space Telescope visual image of the MS0735.6+7421 cluster superposed with the *Chandra* X-ray image in blue and a radio image from the Very Large Array at a frequency of 330 MHz in red. The X-ray image shows an enormous pair of cavities, each roughly 200 kpc in diameter that are filled with radio emission. The radio jets have been inflating the cavities for 10^8 years with an average power of $<2 \times 10^{46}$ erg s^{-1}. The displaced gas mass is $<10^{12}$ $M_\odot$. The cavities and radio source are bounded by a weak shock front. The cavities are well outside the central galaxy and cooling region of the cluster. The supermassive black hole grew by at least $<3 \times 10^8$ $M_\odot$ during the outburst.

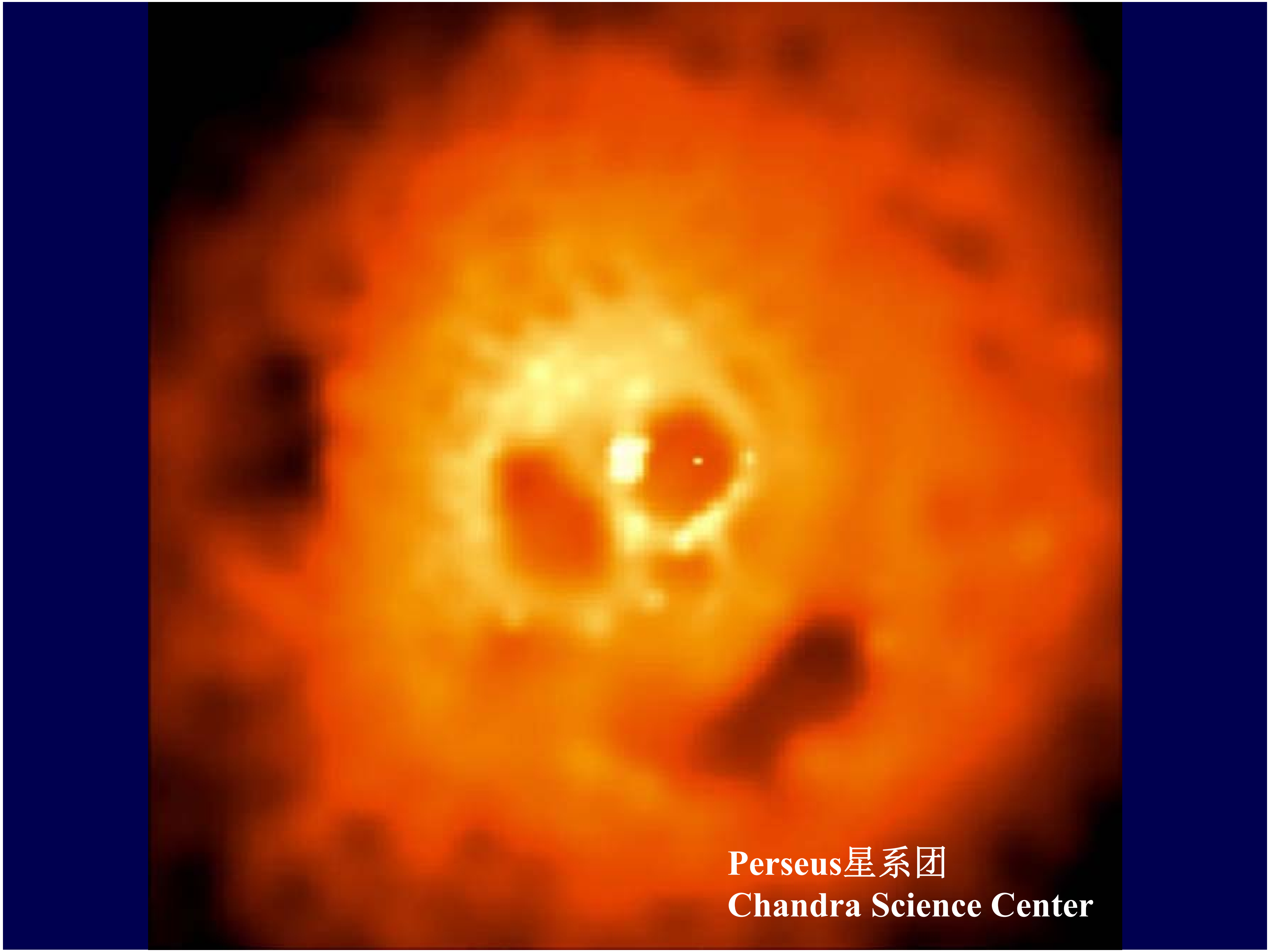
Perseus星系团
Chandra Science Center

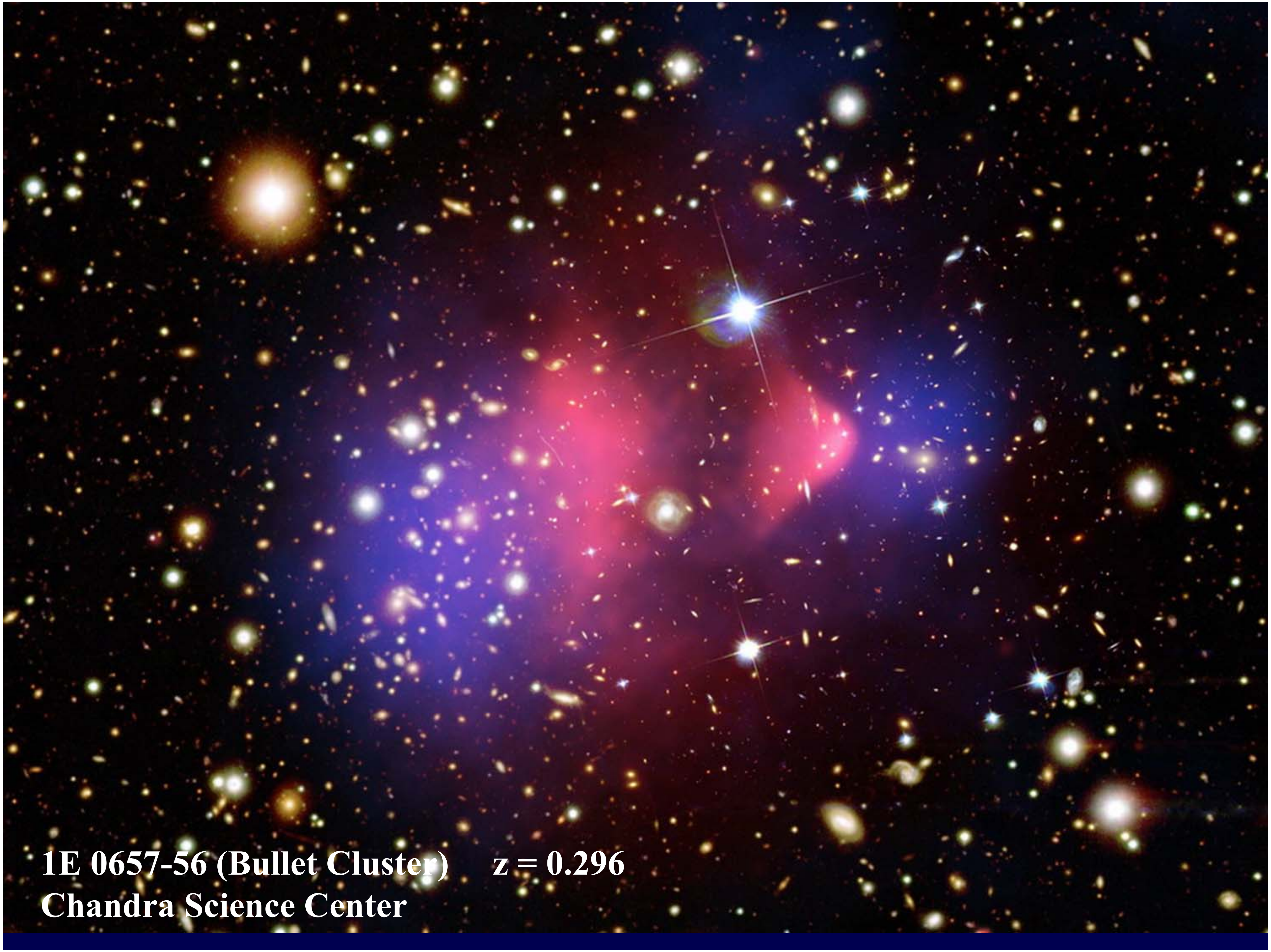
1E 0657-56 (Bullet Cluster) z = 0.296
Chandra Science Center

◆ AGN对ICM加热的贡献

Heating Hot Atmospheres with Active Galactic Nuclei

B.R. McNamara[1,2] and P.E.J. Nulsen[2]

[1]Department of Physics & Astronomy, University of Waterloo, Ontario, Canada, Astrophysical Institute and Department of Physics and Astronomy, Ohio University, Athens, Ohio 45701; email: mcnamara@sciborg.uwaterloo.ca

[2]Harvard-Smithsonian Center for Astrophysics, Cambridge, Massachusetts 02138; email: pnulsen@cfa.harvard.edu

Annu. Rev. Astron. Astrophys. 2007. 45:117–75

First published online as a Review in Advance on May 2, 2007.

The *Annual Review of Astronomy and Astrophysics* is online at astro.annualreviews.org

This article's doi: 10.1146/annurev.astro.45.051806.110625

0066-4146/07/0922-0117$20.00

Key Words

active galactic nuclei, cooling flows, galaxy clusters, radio galaxies, X-ray emission

Abstract

High resolution X-ray spectroscopy of the hot gas in galaxy clusters has shown that the gas is not cooling to low temperatures at the predicted rates of hundreds to thousands of solar masses per year. X-ray images have revealed giant cavities and shock fronts in the hot gas that provide a direct and relatively reliable means of measuring the energy injected into hot atmospheres by active galactic nuclei (AGN). Average radio jet powers are near those required to offset radiative losses and to suppress cooling in isolated giant elliptical galaxies, and in larger systems up to the richest galaxy clusters. This coincidence suggests that heating and cooling are coupled by feedback, which suppresses star formation and the growth of luminous galaxies. How jet energy is converted to heat and the degree to which other heating mechanisms are contributing, e.g., thermal conduction, are not well understood. Outburst energies require substantial late growth of supermassive black holes. Unless all of the $\sim10^{62}$ erg required to suppress star formation is deposited in the cooling regions of clusters, AGN outbursts must alter large-scale properties of the intracluster medium.

对X射线空洞的研究 → 反馈能量估算

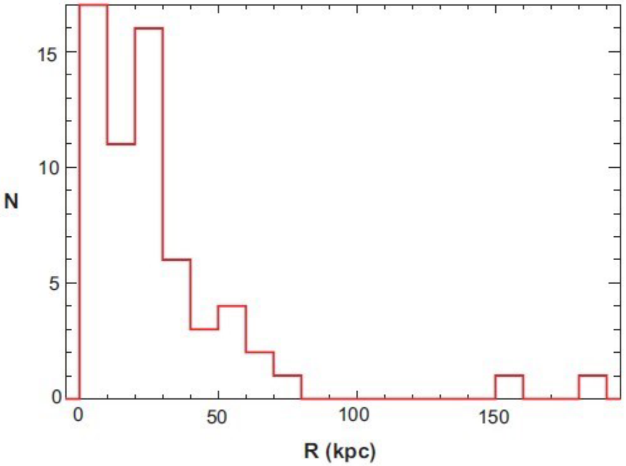

Figure 3
Distribution of cavity distance from the nucleus of the host cD galaxy. Data were taken from Rafferty et al. (2006).

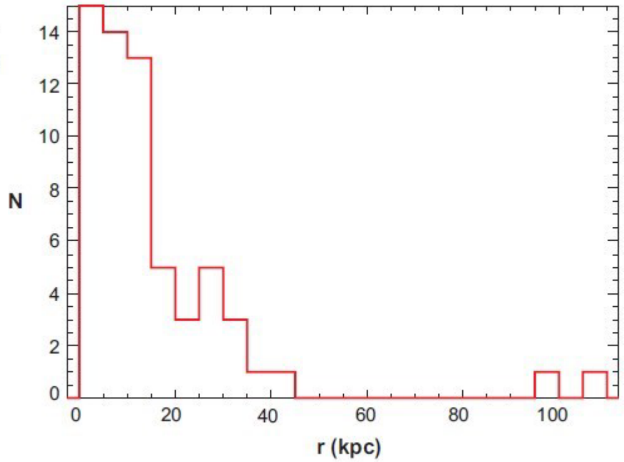

Figure 4
Distribution of cavity sizes. An ellipse was fitted to each cavity and its size is expressed as $\sqrt{ab}$, where a and b are the semiaxes. Data were taken from Rafferty et al. (2006).

Figure 5
Distribution of the ratio of cavity size to nuclear distance. See **Figures 3** and **4**. Data were taken from Rafferty et al. (2006).

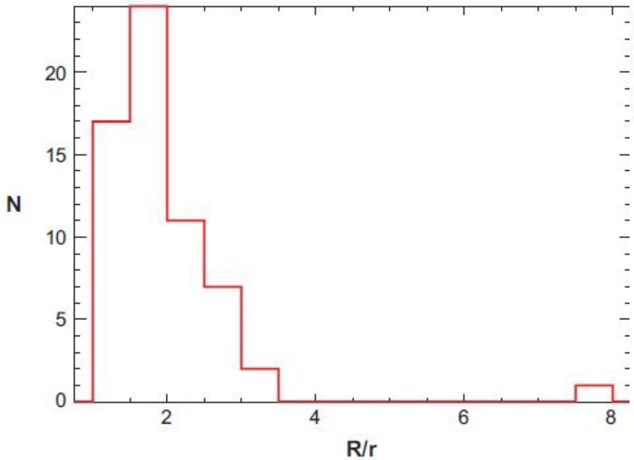

Figure 6
Distribution of cavity buoyancy ages. Data were taken from Rafferty et al. (2006).

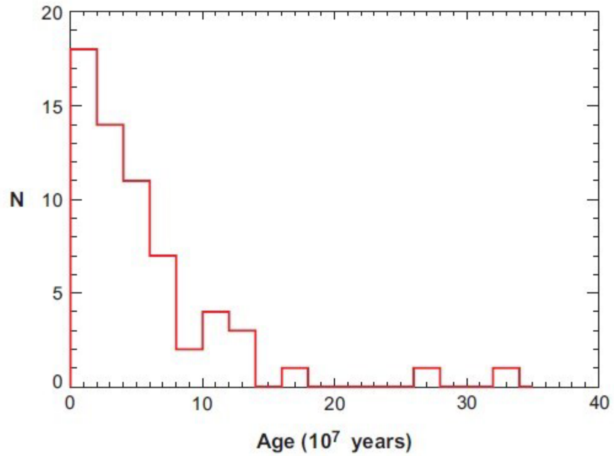

Rafferty et al. 2006 ApJ

喷流的巨大能量供给（辐射能 + 机械能）

Figure 7

Total radio luminosity (10 MHz–10 GHz) plotted against jet power ($4pVt_{\mathrm{bouy}}^{-1}$) taken from Laura Bîrzan's PhD thesis (2007). Open red symbols represent ghost cavities. Solid blue symbols represent radio-filled cavities. The diagonal lines represent ratios of constant jet power to radio synchrotron power. Jet power correlates with synchrotron power but with a large scatter in their ratio. Radio sources in cooling flows are dominated by mechanical power. The radio measurements were made with the Very Large Array telescope.

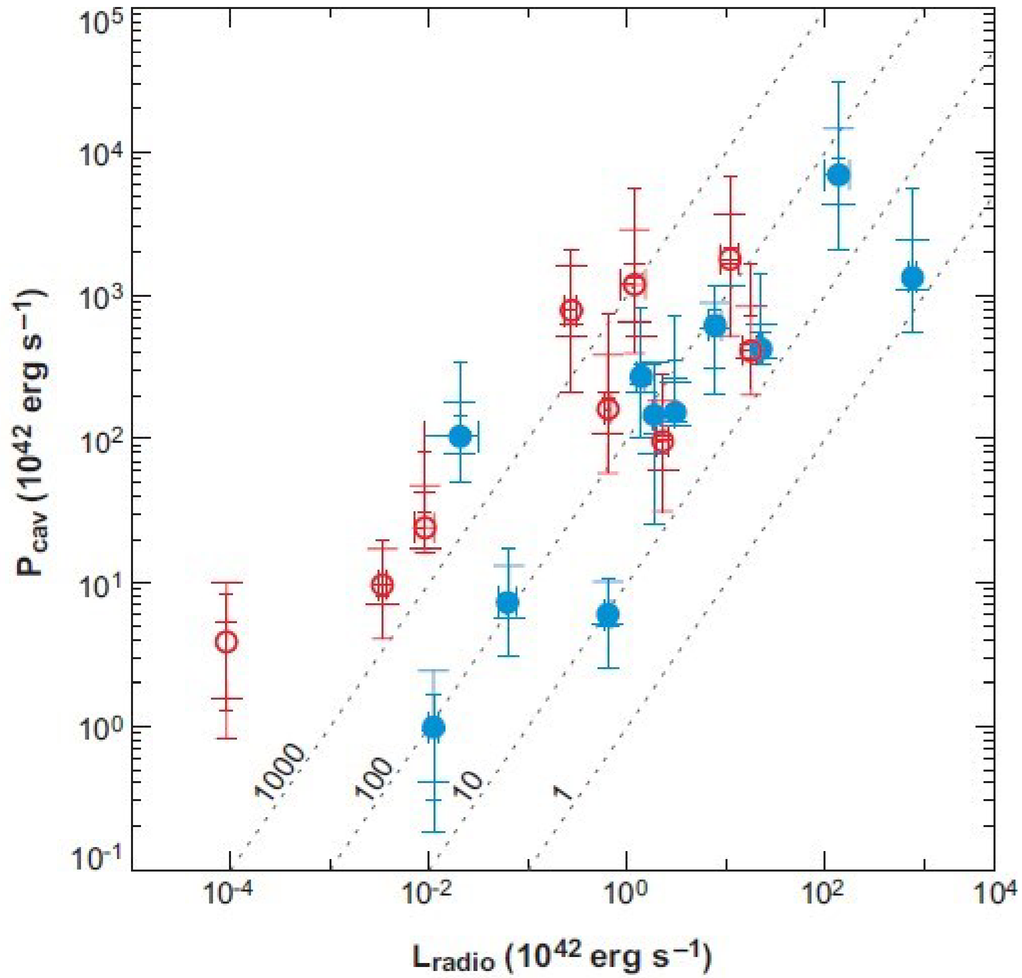

星系团中的喷流功率

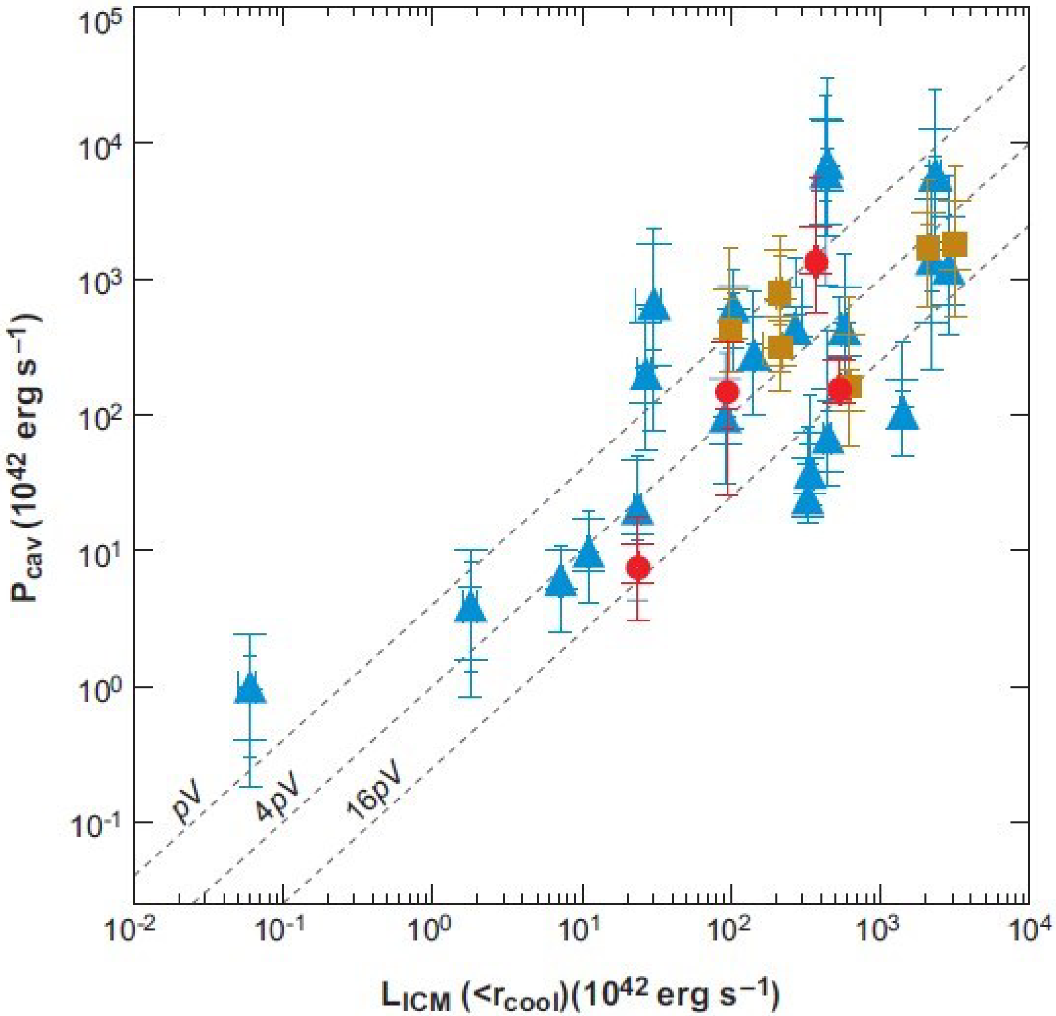

Figure 8

Cavity power of the central AGN plotted against the X-ray luminosity of the intracluster medium (ICM) within the cooling radius, after correcting for mass deposition (Rafferty et al. 2006). The symbols and wide error bars denote values of cavity power calculated using the buoyancy timescale. Short and medium width error bars denote the limits of the cavity power calculated using the sound speed and refill timescales, respectively. Diagonal lines denote equality between heating and cooling rates assuming pV, $4pV$, and $16pV$ of energy per cavity, respectively. Red circles represents well-defined cavities with bright rims, blue triangles represent well-defined cavities without bright rims, and yellow squares represent poorly defined cavities.

椭圆星系中的喷流功率

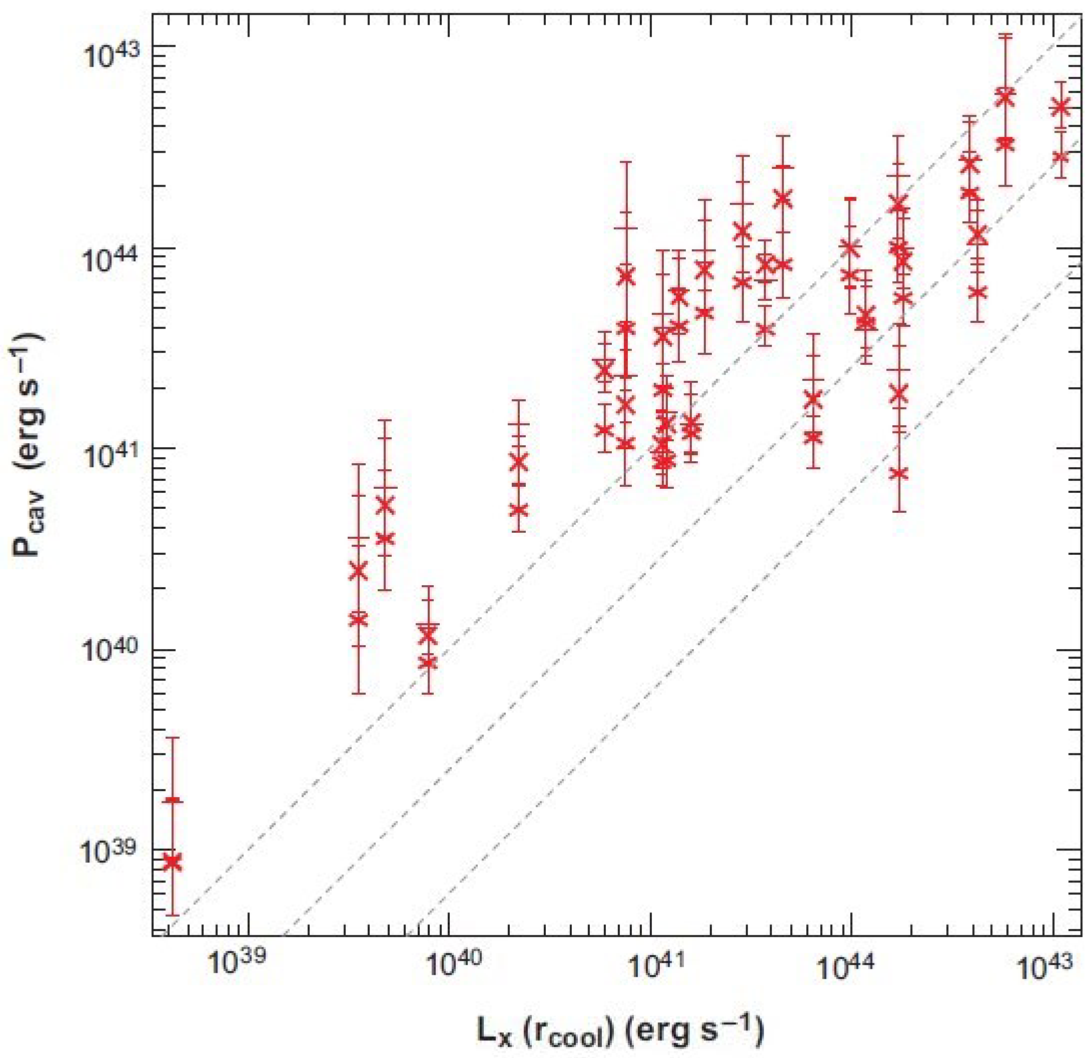

Figure 9

Cavity power versus cooling power for nearby giant elliptical galaxies (Nulsen et al. 2007). Cooling power is the X-ray luminosity from within the projected radius where the cooling time is 7.7×10^9 years. Cavity powers are determined using an energy of pV per cavity and a range of cavity age estimates (see **Figure 8**). The dashed lines show equality for cavity energies of pV, $4pV$, and $16pV$, top to bottom. All but one system lie above the $4pV$ line, indicating that radiative losses can be balanced by AGN power.

部分待解决问题

1、冷流模型的其它解决方案（**star forming**）；

2、如何进一步约束数值模型？

e.g., AGN活动周期？喷流、激波、X射线空洞加热过程的细节？

3、星系群以及早期系统中情况如何？

4、AGN活动与并合的关联；

5、并合过程机械能向内能的转化？

6、金属扩散的问题。

3、AGN活动对星系团的影响II：较时尚话题

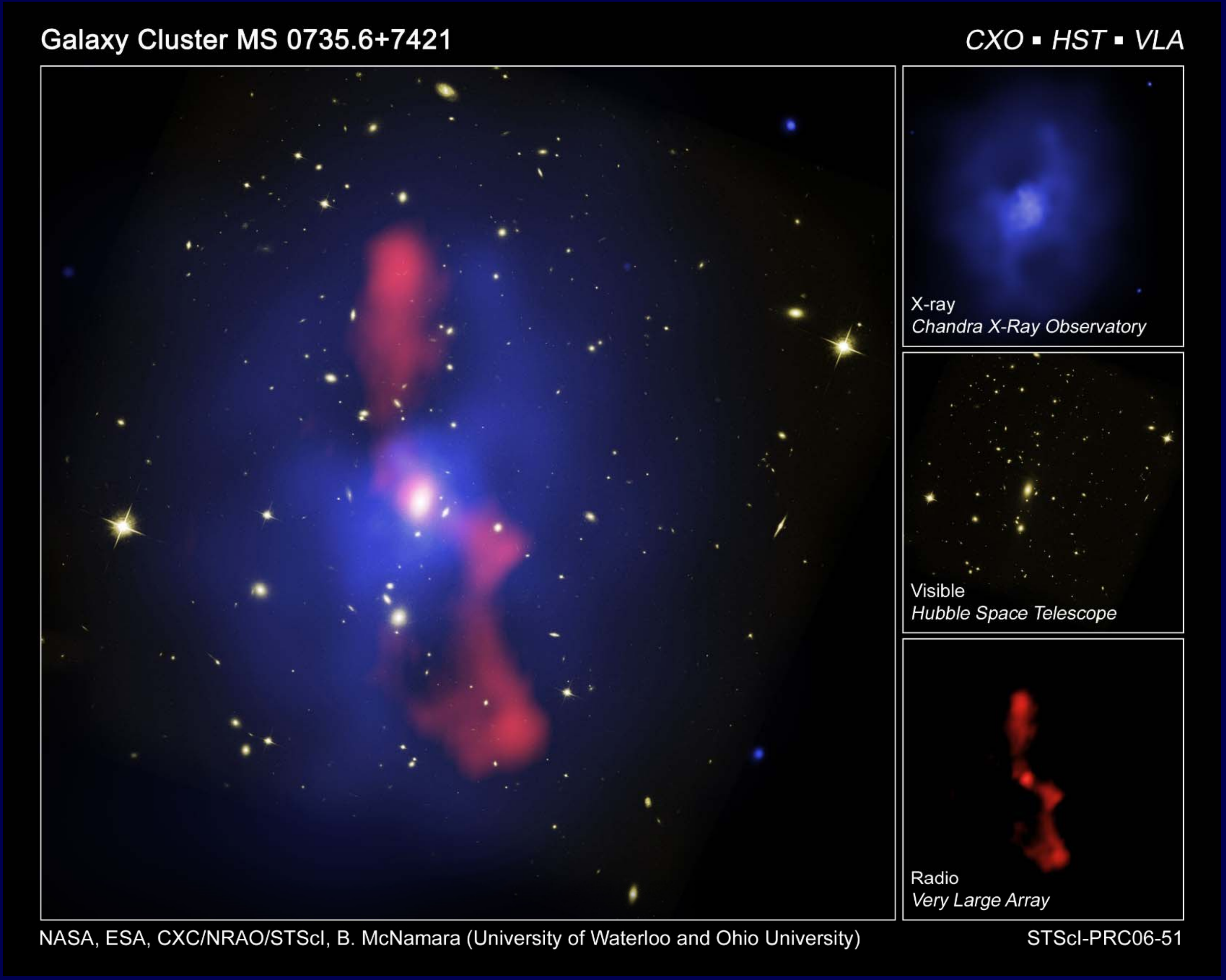

例：MACSJ0717.5+3745中复杂的射电结构
Bonafede et al. 2018 MNRAS

Table 1. MACSJ0717.5+3745

Name	MACSJ0717.5+3745	ref.
RA [J2000]	07h17m30.9s	
DEC[J2000]	37d45′30″	
z	0.546	E01
M_{500}	$(11.5 \pm 0.5) \times 10^{14} M_\odot$	PUC
M_{vir}	$(3.5 \pm 0.6 \times 10^{15} M_\odot$	U14
L_X [0.1 − 2.4keV]	$(2.74 \pm 0.03) \times 10^{45}$ erg/s	E07

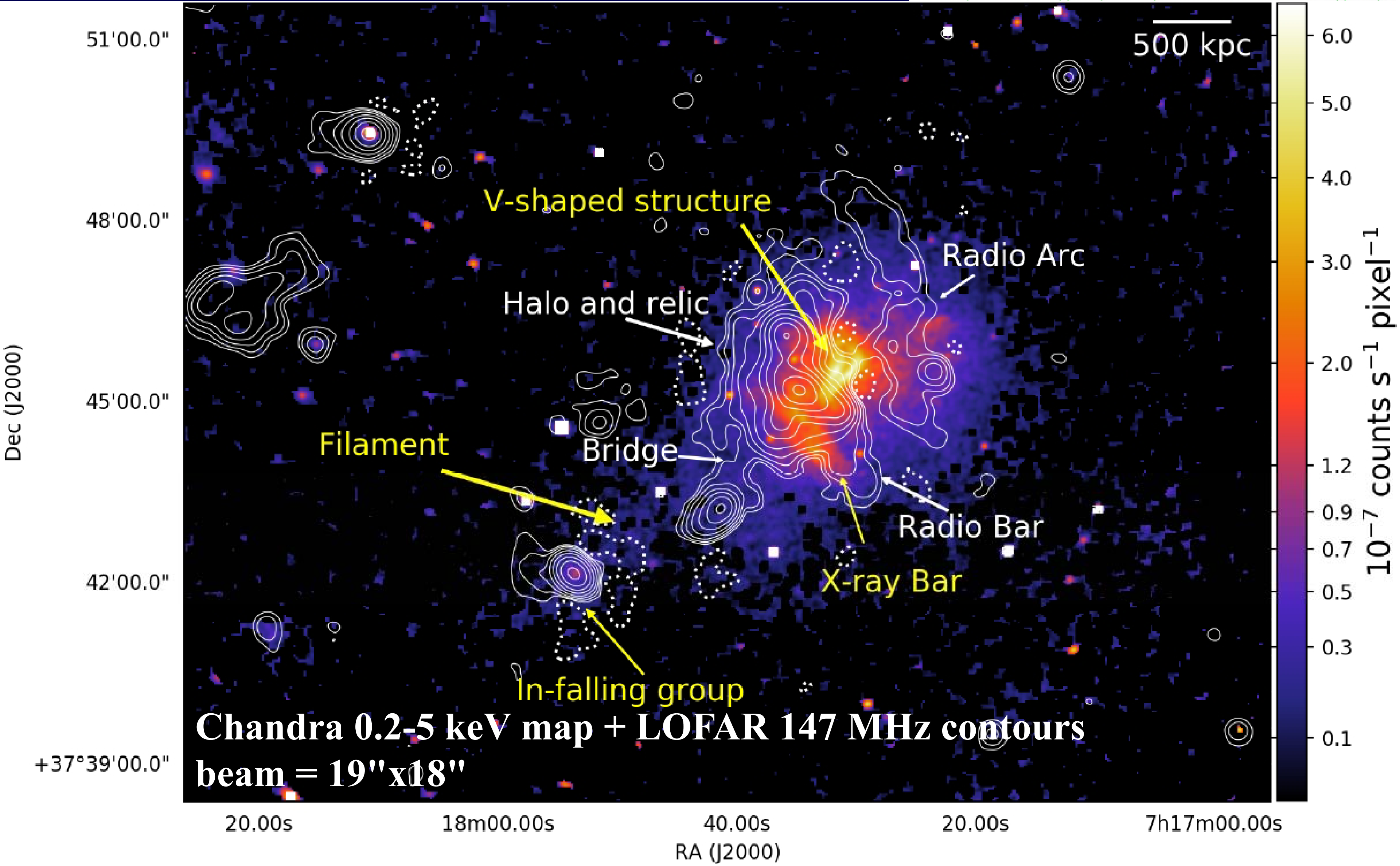

Chandra 0.2-5 keV map + LOFAR 147 MHz contours
beam = 19"x18"

3.1、中低频射电天空中的星系团（群）

ICM中存在空间跨度巨大的弥漫射电源

- 第一例发现于1959年（Coma团中的大型射电晕；Large et al. 1959）；
- 电子$\gamma >> 10^3$ 、$n \sim 10^{-10}$ cm^{-3} 、$u_E < 1\% \ u_{IGM}$、B ~ 0.1-1 μG;
- 成因、位置、形态、谱型、偏振特性等不同于传统AGN产物。

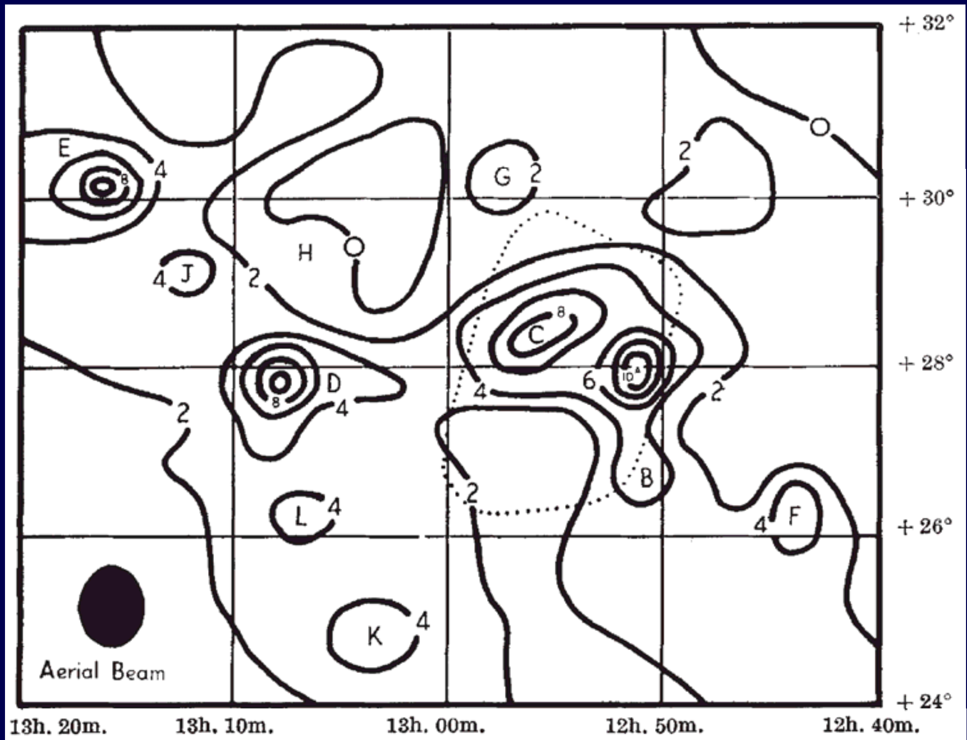

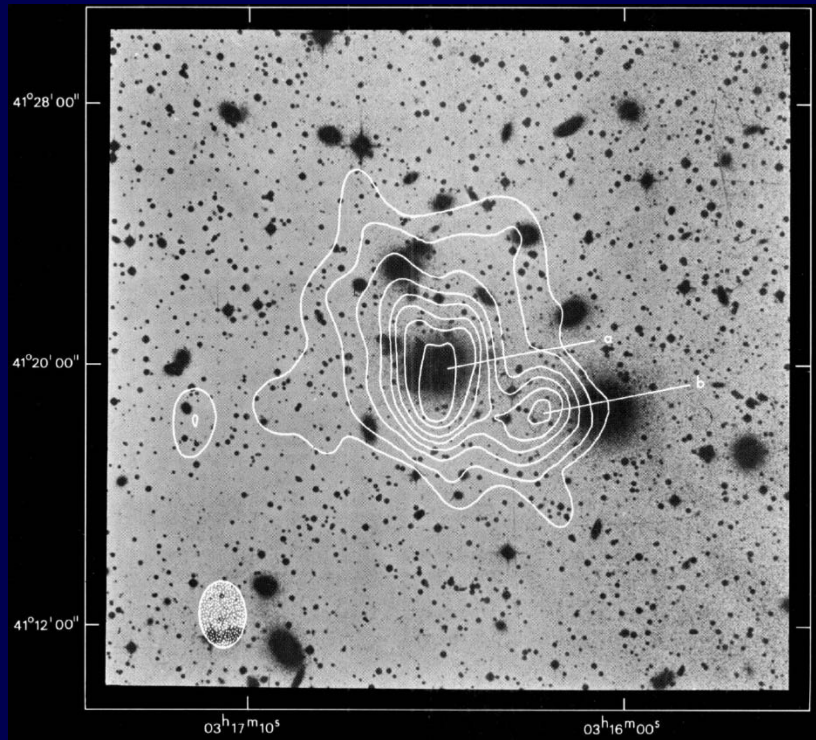

Coma团（308 MHz; Large et al. 1959）以及Perseus团（Miley & Perola 1975）中的大型射电晕

◆ 起因：相对论电子能量损失的两个途径

1、同步辐射；2、对CMB光子的逆康普顿散射

→ 高频部分衰减得比低频部分快

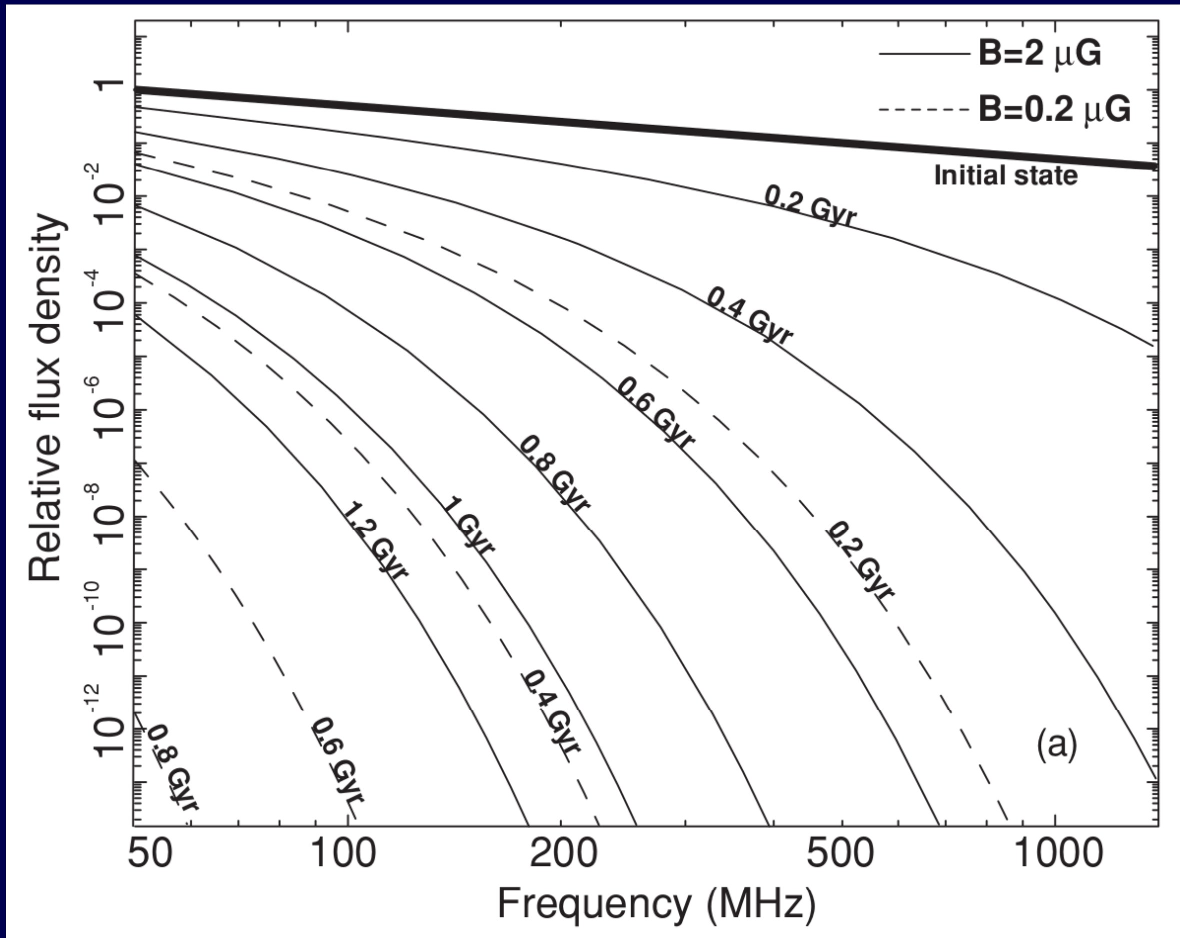

星系团（z=0.2）ICM射电展源的同步辐射谱及其时间演化（Wang et al. 2010）

ICM射电展源的分类和基本特性

- 约三分之一星系团中有复杂的ICM射电展源；
  星系群中极少见，但并不意味着不存在！

类型	星系团类型	位置	尺度量级	形态	偏振
射电晕	并合星系团	中央（非投影效应）	Mpc	规则	无
射电遗迹	并合/弛豫星系团	外围	Mpc	不规则	有（较强）
微射电晕	弛豫冷核星系团	中央（常伴中央射电星系）	数百kpc	规则	无

- 并合/弛豫星系团中，发现ICM射电展源的几率均与L_X相关
  - * $L_X > 5\times10^{44}$ erg s^{-1}的星系团：27-44%有至少一类ICM射电展源
  - * $L_X < 5\times10^{44}$ erg s^{-1}的星系团：6-9%有至少一类ICM射电展源

  Giovannini et al. 1999

第一类：射电晕

- 仅现于并合团（但非所有，例外如**A119**、**A2146**），辐射谱较陡；
- 少数较亮射电晕：谱指数分布现结节、纤维状结构；
- 射电晕与**X**射线气体晕间的明显关联（辐射功率、形态）

例：**A2744**射电晕的较平射电谱子结构与**X**射线高温区有关联、**IGM**温度越高则射电晕频谱越平（**0.3-1.4 GHz**；**Giovannini et al. 2009**）等；

→ 与并合有关的起源？
又因射电晕**Mpc**量级尺度
>> 相对论电子自由程
→ 主并合中的湍流加速

- 几例超陡频谱射电晕（谱指数大于**1.7**）。

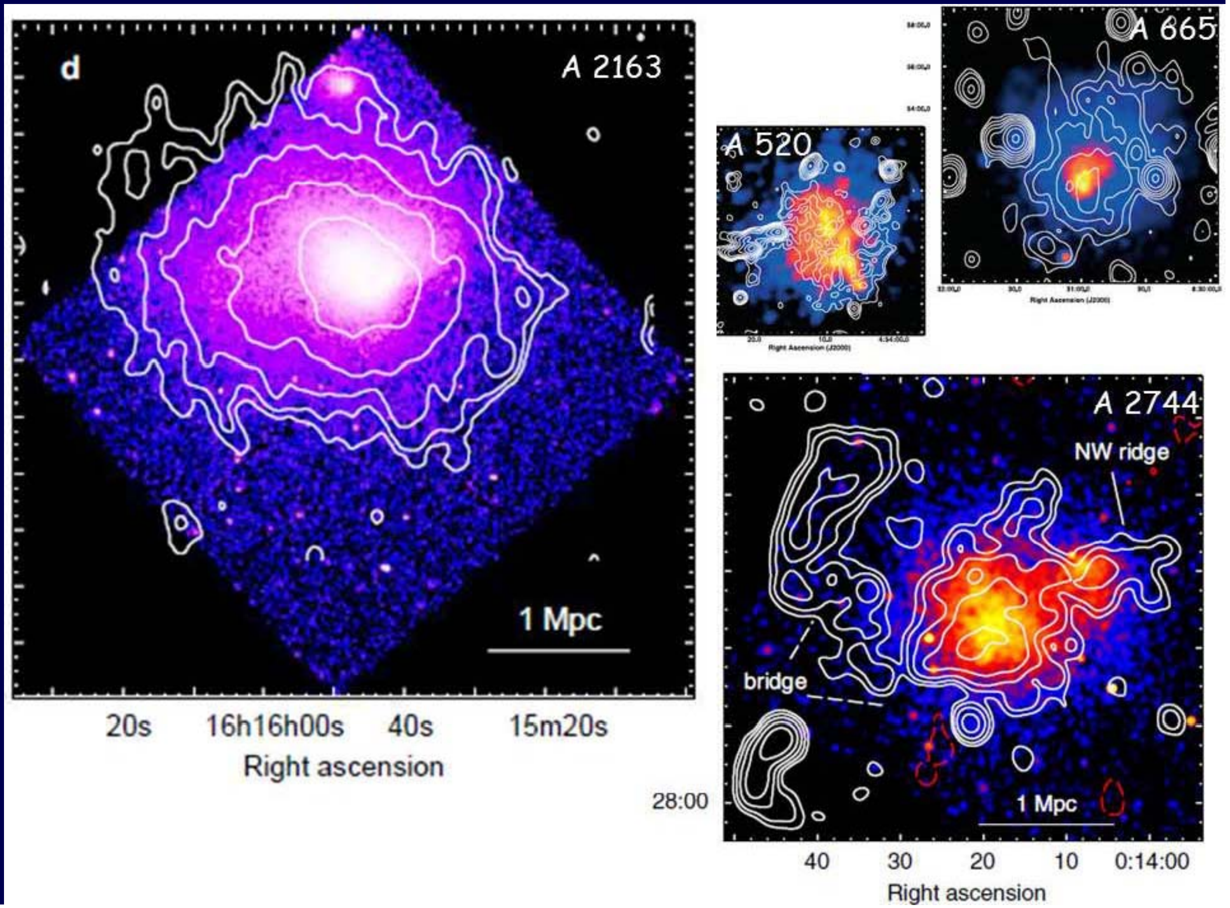

典型射电晕图像（等高线）叠加于**X**射线图像上
Brunetti & Jones 2014

第二类：射电遗迹

- 仅知约50个，多位于富Abell团中；
- 并合星系团、相对弛豫的冷核星系团中均有；

→ 与主、次并合均可能有关

- 频谱较陡且有空间变化；◆ 有明显偏振，常达10-30%（个别更高）；
- 长形（更强更延展、谱指数1-1.6,、位于团外围；与射电晕类似的 1.4 GHz射电功率-星系团X射线光度关联、1.4 GHz射电功率-尺度关联）、 圆形（较弱较小、谱指数1.1-2.9、常居中心及附近）。

→ 长形射电遗迹可能源于并合中的激波加速，而圆形射电遗迹的成因则仍不明

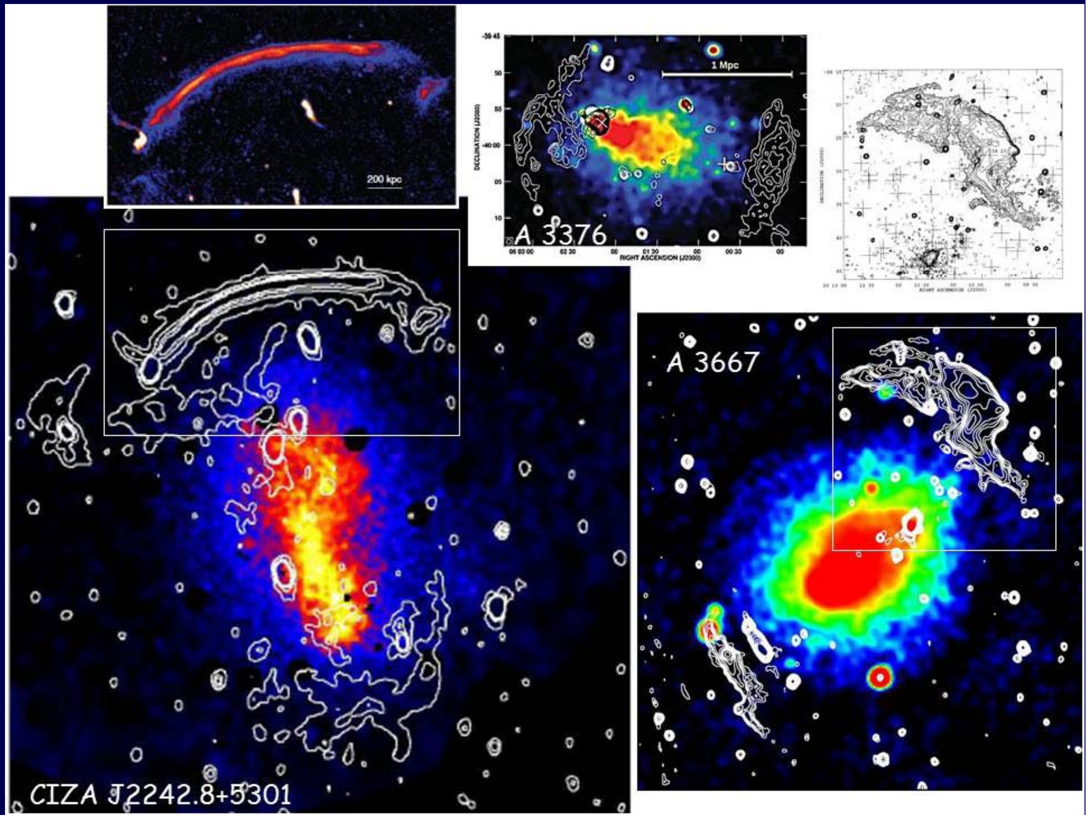

典型射电遗迹图像（等高线）叠加于X射线图像上
Brunetti & Jones 2014

第三类：微射电晕

- 常围绕星系团中央射电星系、延展数百kpc；
- 谱指数类似射电晕、沿径向变陡趋势（如Perseus团；Gitti et al. 2002）；
- 中央射电星系的高能粒子外向扩散不足以影响微射电晕区域、数个微射电晕星系团中现cold front。

→ 冷核星系团中气体sloshing产生的湍流加速、可能与次并合有关

（ZuHone et al. 2013）

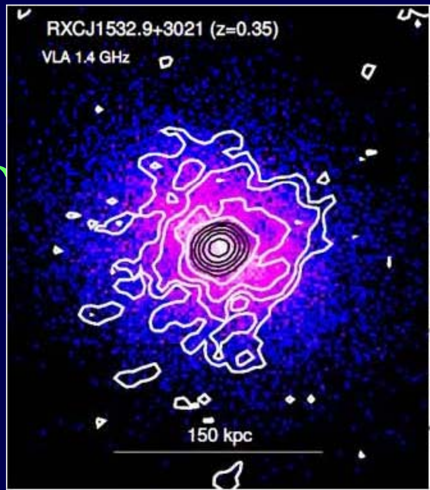

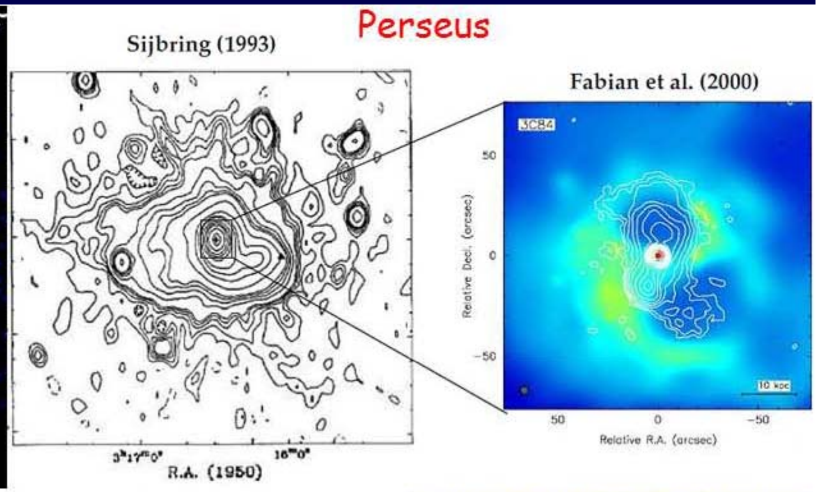

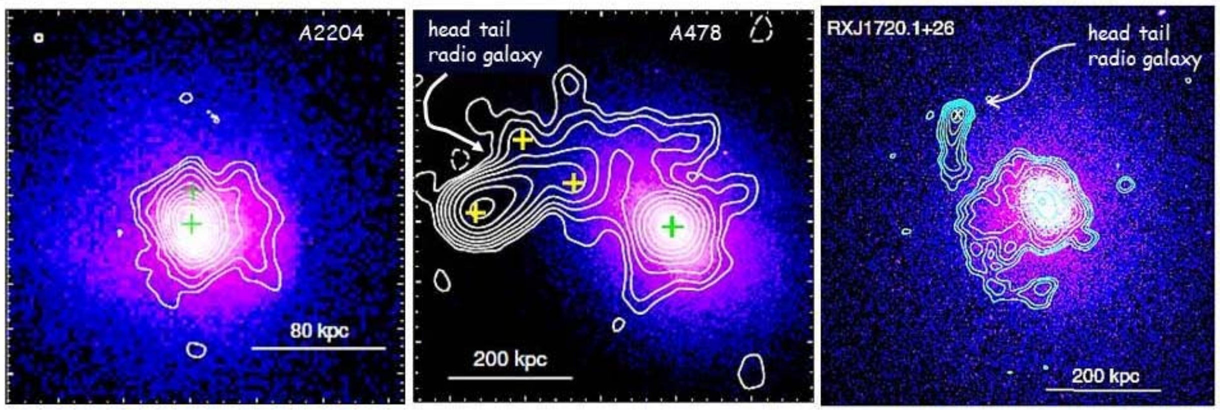

典型微射电晕图像（等高线）叠加于X射线图像上
Brunetti & Jones 2014

ICM射电展源的成因

- 初级电子模型/再加速模型

AGN活动 & 恒星形成活动 → 初级相对论性电子 （??），需再加速！

* 湍流加速

并合 → Mpc尺度湍流 → 共振或非共振碰撞（二阶费米加速），

数个10^8年、$\gamma \sim 10^5$ → 射电晕和微射电晕；

* 激波加速

并合 → 低马赫数（~2-3）激波压缩ICM磁场并使之更加整齐，

初级电子、高能ICM热电子在激波前后来回穿行（一阶费米加速），

→ 长形射电遗迹；

- 次级电子模型/强子模型

* 相对论质子与ICM离子核间非弹性碰撞 → 持续注入次级相对论电子
* 暗物质晕中中微子湮灭 → 高能次级电子

然而，次级电子模型存在一系列问题

* 不能解释射电晕功率-星系团X射线光度关联；
* 不能说明射电遗迹成因；
* 要求较强的ICM磁场（几个甚至数十个μG）；
* 预言几乎所有星系团均有射电晕；
* 预言碰撞过程中因π介子衰变而产生弥漫伽马射线辐射，等；

- 混合模型

3.2、射电桥

并合前星系团对间的弥漫射电结构

Govoni et al. 2020 Science

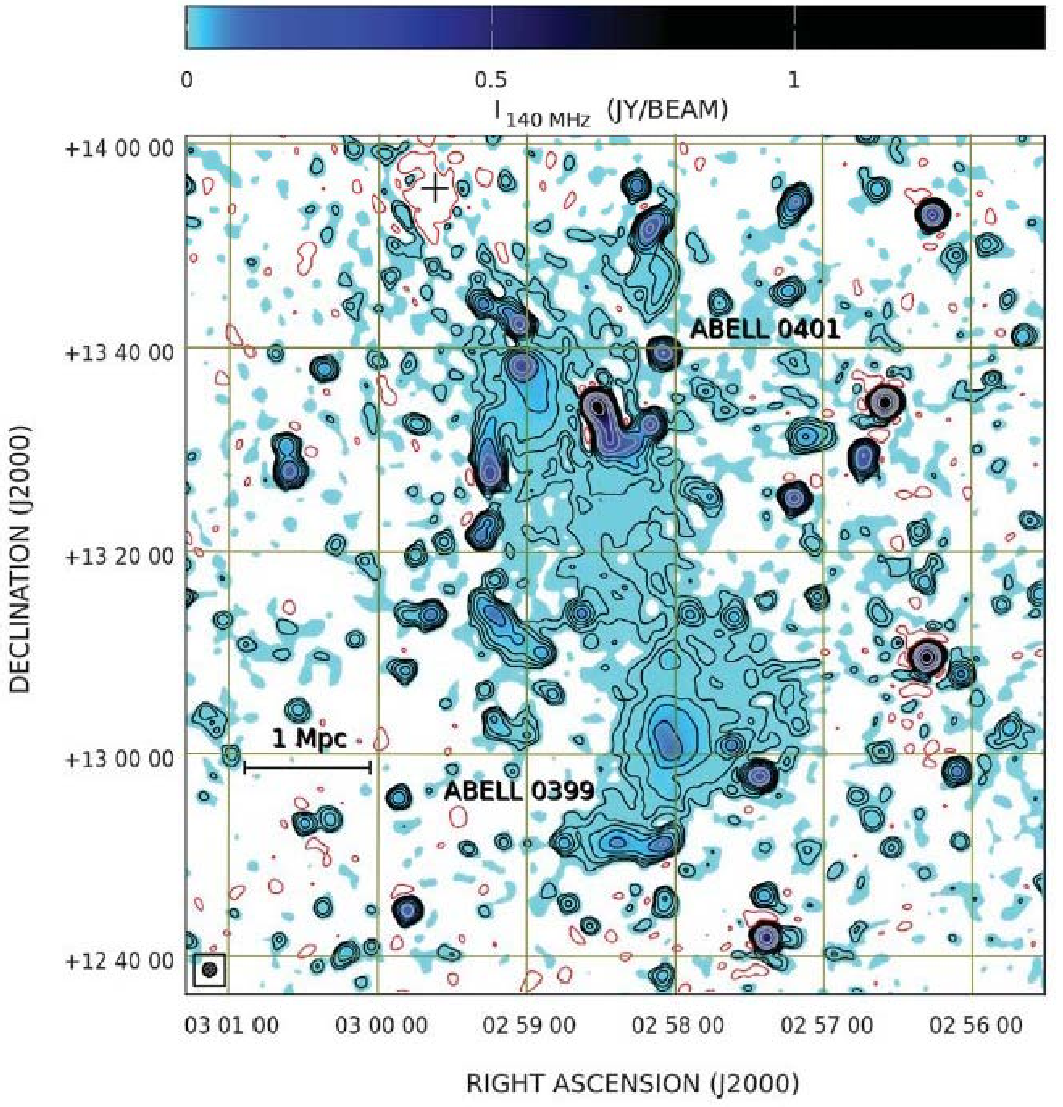

Fig. 1. LOFAR image of the 1.4° × 1.4° region centered on the Abell 0399–Abell 0401 system. Color and contours show the radio emission at 140 MHz with a resolution of 80 arc sec and RMS sensitivity of 1 mJy beam^{-1}. The beam size and shape are indicated by the inset at the bottom left. Contour levels start at 3 mJy beam^{-1} and increase by factors of 2. One negative contour (red) is drawn at −3 mJy beam^{-1}. The black cross (right ascension 02h 59m 38s, declination +13° 54′ 55″, J2000 equinox) indicates the location of a strong radio source that was removed from the image.

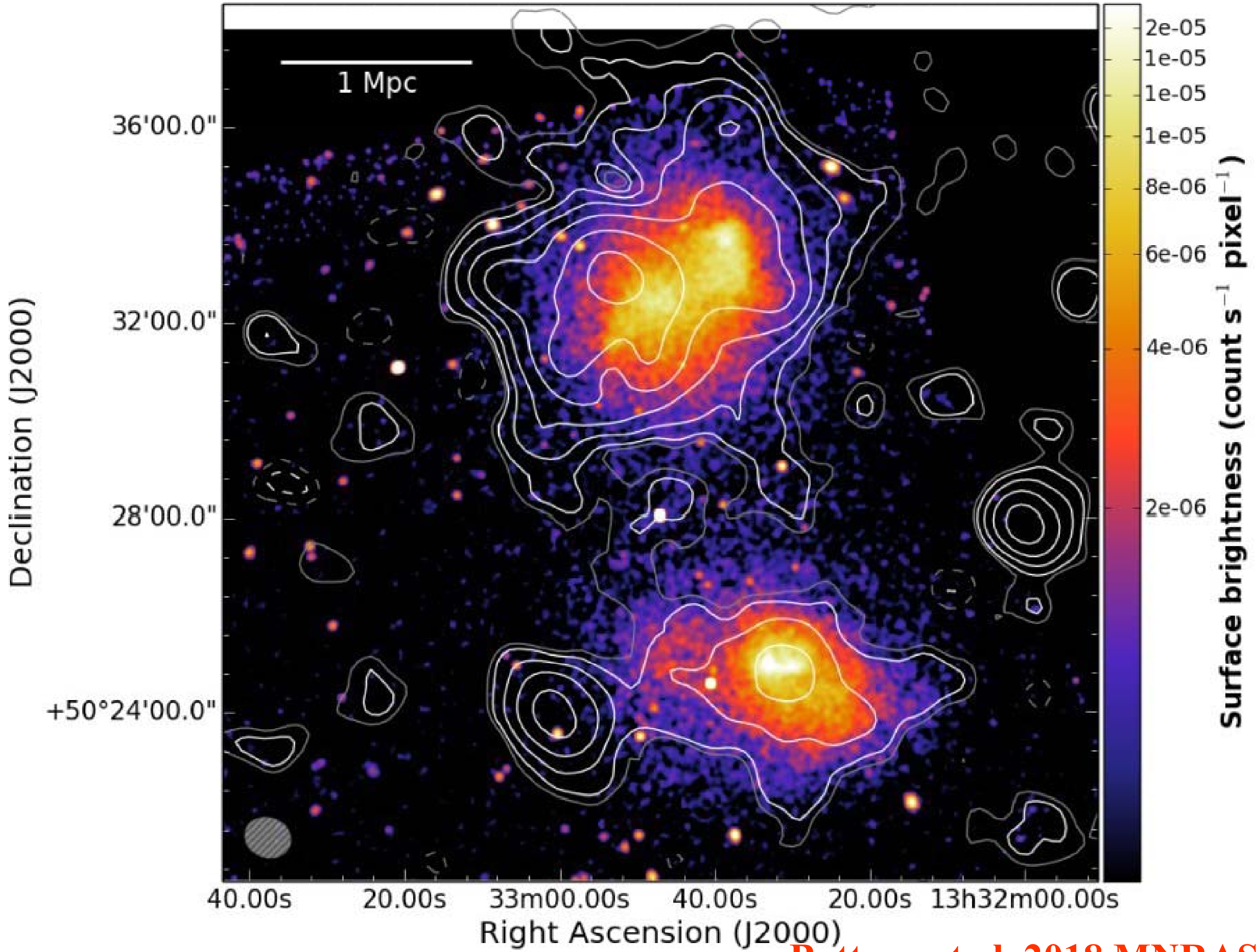

Botteon et al. 2018 MNRAS

Figure 4. LOFAR radio contours with point sources subtracted of A1758 overlaid on the *Chandra* colour image of Fig. 2. The LOFAR white contours are spaced by a factor of 2 starting from 3σ, where $\sigma_{\rm LOFAR}$= 390 μJy beam^{-1}. The negative -3σ contours are shown in dashed. Grey contours correspond to the $\pm 2\sigma$ level. The beam size is 60 arcsec × 51 arcsec and is shown in the bottom left corner. More details on the LOFAR image are reported in Table 2.

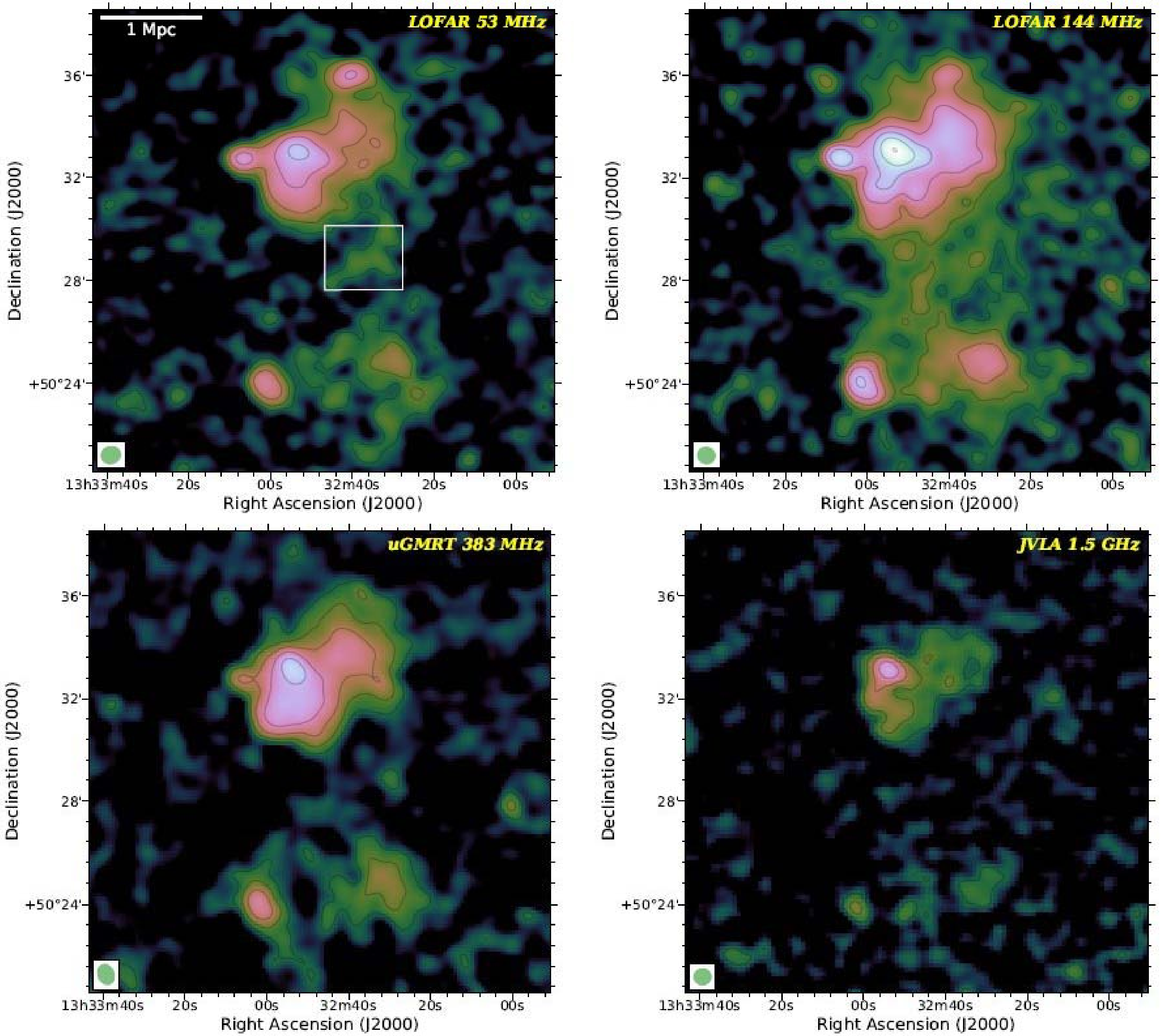

Figure 2. Radio images from 53 MHz to 1.5 GHz of A1758 with discrete sources subtracted. The color scale has a logarithmic stretch from 0.5 to 200σ. Contours are drawn from 3σ and are spaced by a factor of 2, where $\sigma_{53\,\mathrm{MHz}} = 1.6$ mJy beam^{-1}, $\sigma_{144\,\mathrm{MHz}} = 160$ μJy beam^{-1}, $\sigma_{383\,\mathrm{MHz}} = 170$ μJy beam^{-1}, $\sigma_{1.5\,\mathrm{GHz}} = 80$ μJy beam^{-1}. Images were obtained by applying a Gaussian uv-taper of 35″; restoring beams are shown in the bottom left corners. The white box denotes the region where we measured a spectral index of $\alpha = 1.65 \pm 0.27$ between 53 and 144 MHz.

Botteon et al. 2020 MNRAS

	Abell 399 - Abell 401 pair		Abell 1758 pair	
	Abell 399	**Abell 401**	**A 1758N**	**A 1758S**
R.A. (2000.0) (hh mm ss.s)	02 57 56.4	02 58 57.5	13 32 44.8	13 32 30.2
Decl. (2000.0) (dd mm ss)	+13 00 59	+13 34 46	+50 32 24	+50 24 32
z	0.0724	0.0737	0.279	0.280
M_{500} (10^{14} $M_{\odot}$)	5.7	9.3	8.0	5.1
R_{500} (Mpc)	1.31	1.62	2.6 (R_{200})	2.2 (R_{200})
T (keV)	7.23	8.47	~ 9	~ 6
Merger	Yes	Yes	Yes	Yes
	Bridge in Abell 399 - Abell 401 pair		**Bridge in Abell 1758 pair**	
Bridge separation d_{proj} (Mpc)	~ 3		~ 2	
d_{proj} (arcmin)	~ 20		~ 6	
Bridge temperature T (keV)	~ 6-7		~ 7.5	
Bridge gas density n_e (cm^{-3})	3×10^{-4}		---	
Mach number of the shock	< 2		~ 3	

Table1. Basic properties of the two proto-type radio bridge pairs. Values are taken from Govoni et al. (2019) for the pair Abell 399 – Abell 401 and Botteon et al. (2018) for the pair Abell 1758.

◆ 研究射电桥的意义

约束星系团并合模型；维里半径区物理（如磁场）

纤维结构与失踪重子，**etc.**

	Abell 3016 - Abell 3017 pair		Abell 222 - Abell 223 pair	
	Abell 3016	**Abell 3017**	**Abell 222**	**Abell 223**
R.A. (2000.0) (hh mm ss.s)	02 25 22. 1	02 25 52.2	01 37 29.2	01 37 56.4
Decl. (2000.0) (dd mm ss)	-42 00 30	-41 54 31	-12 59 10	-12 48 01
z	0.219	0.219	0.213	0.207
M_{500} ($10^{14} M_{\odot}$)	2.6	7.0	3.0 (M_{200})	5.3 (M_{200})
R_{500} (Mpc)	0.9	1.2	1.28 (R_{200})	1.55 (R_{200})
T (keV)	3.92	7.05	4.43	5.31
Merger	no	yes	no	yes
	Bridge in Abell 3016 - Abell 3017 pair		**Bridge in Abell 222 - Abell 223 pair**	
Bridge separation d_{proj} (Mpc) d_{proj} (arcmin)	~ 1 ~ 4.7		~ 2.8 ~ 14	
Bridge gas temperature T (keV)	~ 4.14		~ 0.91	
Bridge gas density n_e (cm^{-3})	8.2×10^{-4}		$< 1\times10^{-4}$	

Table2. Basic properties of targets of galaxy cluster pairs. Values are taken from Chon et al. (2019) for the pair of Abell 3016 – Abell 3017 and Werner et al. (2008) for the Abell 222 – Abell 223.

Hu et al. 2020
170 hr MWA time granted

部分待解决问题

1、低质量并合系统中有无射电晕和射电遗迹？

2、射电桥是否是并和前的特征现象？

3、相对论电子的来源为何？与AGN有何关联？

4、如何利用这些现象约束磁场？

5、微射电晕是AGN的直接产物吗？

敬请批评指正！